

**Lu-Hf AND Sm-Nd AGES AND SOURCE COMPOSITIONS FOR DEPLETED  
SHERGOTTITE TISSINT**

---

A Thesis Presented to the Faculty of the  
Department of Earth and Atmospheric Sciences  
University of Houston

---

In Partial Fulfillment  
of the Requirements for the Degree  
Master of Science

---

By  
Therica Esther Grosshans

December 2013

**Lu-Hf AND Sm-Nd AGES AND SOURCE COMPOSITIONS FOR DEPLETED  
SHERGOTTITE TISSINT**

---

**Therica Esther Grosshans**

APPROVED:

---

**Dr. Thomas Lapen, Advisor**

---

**Dr. Alan Brandon**

---

**Dr. Rasmus Andreasen**

---

**Dr. Kevin Righter, Johnson Space Center**

---

**Dr. Dan Wells, Dean  
College of Natural Sciences and Mathematics**

## ACKNOWLEDGEMENTS

First, I would like to thank my advisor, Dr. Tom Lapen, for the opportunity to work on such a great project. Thank you for your time, guidance, and sharing your knowledge with me through the last few years. Next, I would like to thank my committee members. Thank you to Dr. Alan Brandon and Dr. Kevin Righter for your support and assistance throughout the course of my work. Thank you to Dr. Rasmus Andreasen for all your assistance on the MC-ICP-MS and involvement with my research. All your help, especially at 4 a.m. when the machine would stop running, during my research is much appreciated.

Thank you to Dr. Minako Righter, Barry Shaulis, and Jesse Dietderich for their assistance with the LA-ICP-MS and spending a lot of your time helping me in the clean lab. We successfully made it through this research without an acid burn. However, some special glassware did not.

A special thanks to my parents, Mike and Christie, and my sisters, Erin and Alicia, for their love and support while in school. I would also like to thank my friends for helping me get through stressful times and cheering me up at the times I needed it. I love you all.

Thank you to Anne Peslier, Kent Ross, and Cherie Achilles at NASA Johnson Space Center for their help with my sample and the SEM and EMPA machines. I would like to also acknowledge this research was funded by the NASA Mars Fundamental Research Program.

Thank you again to everyone mentioned above and anyone I may have forgotten. I would not have been able to finish my thesis with a sane mind without your help, support, and encouragement.

**Lu-Hf AND Sm-Nd AGES AND SOURCE COMPOSITIONS FOR DEPLETED  
SHERGOTTITE TISSINT**

---

An Abstract of a Thesis

Presented to the Faculty of the  
Department of Earth and Atmospheric Sciences  
University of Houston

---

In Partial Fulfillment  
of the Requirements for the Degree  
Master of Science

---

By

Therica Esther Grosshans

December 2013

## ABSTRACT

Tissint is the fifth witnessed Martian meteorite fall and was collected in Morocco in 2011. The quick recovery of this meteorite limits the possibility of terrestrial weathering or contamination by terrestrial components. Tissint is classified as a depleted olivine-phyric shergottite similar in bulk composition to Dar al Gani 476 and EETA79001A. It has a porphyritic texture with primary mineral phases of olivine, plagioclase (maskelynite), and pyroxene (augite and pigeonite). Other phases include oxides (chromite, ilmenite, magnetite) and phosphate (Irving et al., 2012).

*In situ* trace element analyses of plagioclase and pyroxene show a depletion of light REE relative to heavy REE, similar to bulk Tissint and other depleted shergottites. Microprobe analyses indicate that the core compositions of macrocrystic olivine were likely in equilibrium with the melt from which they crystallized. Oxybarometry calculations utilizing equilibrium olivine-pyroxene-spinel and late-stage oxides reveal that the Tissint melt became oxidized during crystallization.

The plagioclase, pyroxene, and whole rock fractions yielded Lu-Hf and Sm-Nd ages of  $570 \pm 84$  Ma and  $690 \pm 140$  Ma, respectively. The initial  $^{176}\text{Hf}/^{177}\text{Hf}$  isotope ratio is  $0.284060 \pm 0.000046$  and the initial  $^{143}\text{Nd}/^{144}\text{Nd}$  isotope ratio is  $0.51376 \pm 0.00034$ . Using the weighted average of all internal isochron ages ( $597 \pm 27$  Ma) and whole rock isotope compositions, initial  $\epsilon^{176}\text{Hf}$  and  $\epsilon^{143}\text{Nd}$  are calculated to be  $+57.8 \pm 0.9$  and  $+41.6 \pm 1.5$ , respectively. Initial  $\epsilon^{176}\text{Hf}$  and  $\epsilon^{143}\text{Nd}$  values and calculated  $^{176}\text{Lu}$ - $^{177}\text{Hf}$  and  $^{147}\text{Sm}$ - $^{144}\text{Nd}$  source ratios of 0.0548 and 0.279, respectively, indicate Tissint is the most depleted in incompatible trace elements of known shergottites and was derived from one of the most depleted sources of shergottites that has been recognized.

The Lu-Hf and Sm-Nd internal isochron ages of this study are consistent with previously published Sm-Nd and Rb-Sr (Brennecka et al., 2012; 2013) and Ar-Ar (Park et al., 2013) ages. These ages indicate Tissint is one of the oldest known shergottites, except possibly for Dhofar 019 which is  $586 \pm 9$  Ma (Borg et al., 2001).

# Table of Contents

<b>Introduction</b>	<b>1</b>
<b>Sample Descriptions</b>	<b>6</b>
<b>Methods</b>	<b>9</b>
<b>3.1 Thick section</b>	<b>9</b>
3.1.1 Scanning Electron Microscope (SEM)	9
3.1.2 Electron Probe Micro Analyses (EPMA)	10
3.1.3 Laser Ablation Inductively Coupled Plasma Mass Spectrometry (LA-ICP-MS)	10
<b>3.2 Interior Sample and Whole Rock Powder</b>	<b>11</b>
3.2.1 Sample Preparation	11
3.2.2 Sample Digestion	12
3.2.3 Ion-exchange chromatography	13
3.2.4 Multi-collector Inductively Coupled Mass Spectrometry (MC-ICP-MS)	14
<b>Results</b>	<b>16</b>
<b>4.1 Electron Probe Microanalyses</b>	<b>16</b>
<b>4.2 REE Concentrations</b>	<b>20</b>
<b>4.3 Lu-Hf and Sm Nd Isochrons</b>	<b>23</b>
4.3.1 $^{176}\text{Lu}$ - $^{176}\text{Hf}$ Isochron	23
4.3.2 $^{147}\text{Sm}$ - $^{143}\text{Nd}$ Isochron	26
<b>Discussion</b>	<b>28</b>
<b>5.1 Composition</b>	<b>28</b>
5.1.1 Pyroxene	28

5.1.2 Olivine	30
5.1.3 Plagioclase	31
5.1.4 Oxides	32
<b>5.2 Crystallization Ages</b>	<b>36</b>
<b>5.3 Source Compositions</b>	<b>40</b>
5.3.1 $\epsilon^{176}\text{Hf}$ and $\epsilon^{143}\text{Nd}$	40
5.3.2 Source Composition	40
<b>5.4 Martian Mantle Sources</b>	<b>44</b>
<b><i>Conclusion</i></b>	<b>47</b>
<b><i>References</i></b>	<b>49</b>
<b><i>Appendices</i></b>	<b>59</b>

# List of Figures, Tables, and Equations

## Figures

1	Hand specimens of Tissint collected in Morocco in 2011	2
2	Mixing curves for calculated source compositions for Martian meteorites	3
3	Mixing diagram for $^{147}\text{Sm}/^{144}\text{Nd}$ and $^{176}\text{Lu}/^{177}\text{Hf}$ source compositions of shergottites and orthopyroxenite ALH 84001	5
4	Backscatter image of a thick section of Tissint using a JEOL JSM-7600F FE-SEM	8
5	Elemental compositions of the major constituent phases	20
6	Chondrite normalized REE abundances for Tissint phases, bulk Tissint, and other depleted shergottites	22
7	Lu-Hf isochron	25
8	Sm-Nd isochron	27
9	Fe vs. Mn for olivines and pyroxenes	29
10	Bulk Mg# plotted against Fo content of olivine macrocryst cores for olivine-phyric shergottites	31
11	Comparison of La/Yb vs $\text{K}_2\text{O}/\text{Na}_2\text{O} \times \text{Al}_2\text{O}_3$ for plagioclase in Tissint and other shergottites	32
12	Weighted average for all internal isochron ages	38
13	Sm-Nd ages for shergottites	39
14	Mixing diagram for shergottites and ALH 84001	42

## Tables

1	Average composition for pyroxene, olivine, and plagioclase	18
2	Average composition for oxides and phosphates	19
3	Lu and Hf data for Tissint	26
4	Sm and Nd data for Tissint	30
5	Oxybarometry results	36
6	Ages determined for Tissint from previously published data and this study	38
7	Ages and isotope data for Tissint and other shergottites	43

## Equations

1	Isochron age	23
2	Initial $\epsilon_{\text{Hf}}$	23
3	Initial $\epsilon_{\text{Nd}}$	23
4	Olivine-melt Fe-Mg exchange coefficient ( $K_D$ )	30
5	Source isotope composition	40

# Chapter 1

## Introduction

Shergottites are a group of meteorites that are part of the Shergotty-Nakhla-Chassigny (SNC) suite of Martian meteorites. The first meteorite to be identified as Martian was the shergottite Elephant Moraine 79001 (EET A79001). The composition of the trapped gases matched the composition of the Mars atmosphere measured from the 1976 NASA Viking lander (Bogard and Johnson, 1983). Shergottites are named after the meteorite Shergotty that was a witnessed fall in India in 1865 (McSween and Treiman, 1998). These rocks are basaltic in composition and their crystallization ages range from 165-586 Ma (Borg et al., 2001; Nyquist et al., 2001; Lapen et al., 2010). These meteorites have been further categorized into enriched, intermediate, and depleted shergottites based on their trace element compositions and initial isotopic compositions (Borg et al., 2003). Studies of these rocks have been useful in trying to understand the history of Mars, the compositions of mantle sources, and the evolution of Martian mantle reservoirs.

Tissint is the fifth witnessed meteorite fall to be identified as Martian. The fall was observed on July 18, 2011 in Morocco. Nomads and the local people began

discovering fragments of the meteorite a few months after the fall with the mass totaling over 12 kilograms. Fig. 1a shows a fresh hand sample of Tissint exhibiting the fusion crust that formed during the meteorite's entry into the Earth's atmosphere and Fig. 1b shows the light gray interior of a hand sample. Small, thin glass veins that likely formed during the impact ejection event occur throughout the stone. The relatively quick recovery of this meteorite limits the degree of weathering and contamination by terrestrial components. Tissint is similar in mineralogical and rare earth element (REE) composition to olivine-phyric shergottites Dar al Gani 476 (DaG 476) and EET A79001 Lithology A. The major mineralogical components of Tissint are plagioclase (maskelynite), pyroxene, and olivine. Based on mineralogical and isotopic compositions, Tissint has been determined to be a depleted olivine-phyric shergottite (Irving et al., 2012; Chennaoui Aoudejeane et al., 2012). Tissint's ejection age of  $1.10 \pm 0.15$  Ma is similar to those for other depleted olivine-phyric shergottites, and suggests that a single impact event ejected several depleted shergottites together (Nishiizumi et al., 2012).

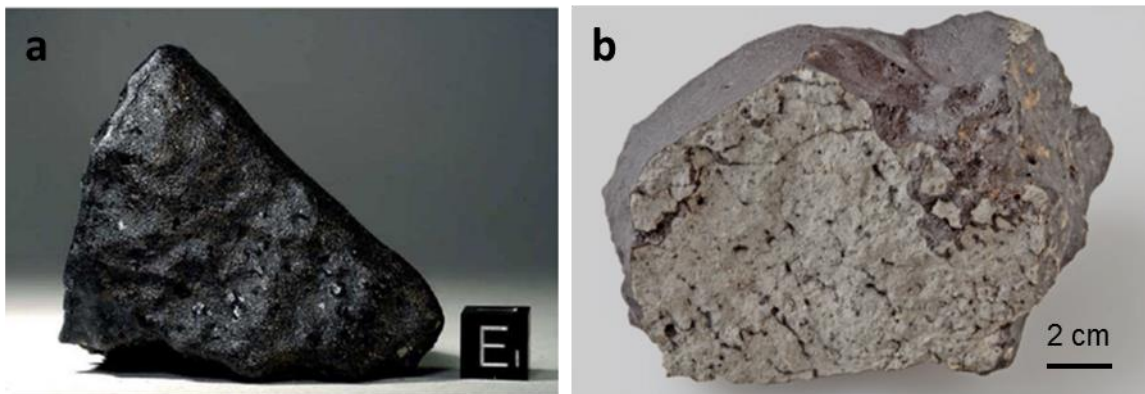


**Fig. 1.** Hand specimens of Tissint collected in Morocco in 2011. (a) 147 gram stone with noticeable black fusion crust. Die is 1 cm x 1 cm x 1 cm. (Irving et al., 2012) (b) A look at the fresh interior of Tissint. The small black veins through the groundmass are glass veins. (Mustard et al., 2013)

Brennecka et al. (2012) reported a  $^{143}\text{Nd}$ - $^{144}\text{Nd}$  age of  $596 \pm 23$  Ma and an initial  $\epsilon^{143}\text{Nd}$  value of +41.9. The values were calculated from the isotopic compositions for a whole rock leachate, a whole rock residue, and an unleached whole rock sample.

Brennecka et al. (2013) presented  $^{87}\text{Rb}$ - $^{87}\text{Sr}$  and  $^{147}\text{Sm}$ - $^{143}\text{Nd}$  ages of  $560 \pm 30$  Ma and  $590 \pm 12$  Ma, respectively, and a weighted average age of  $580 \pm 18$  Ma. These two isochrons were calculated from internal isochrons of mineral separates.

Previous studies have shown that the Rb-Sr and Sm-Nd isotopic systems are susceptible to resetting during impact and terrestrial weathering (e.g., Borg et al., 2001; 2003). Lapen et al. (2010) demonstrated that the Lu-Hf system is more robust than the other two systems because it is resistant to phosphate alteration. Phosphate can host the majority of Sm and Nd in a sample. Internal isochrons can be affected if these elements become mobile during impact or weathering.

Martian meteorite source compositions and evolution of Martian mantle reservoirs have important implications for understanding planetary evolution. Borg et al. (2003) introduced a binary mixing model for  $^{87}\text{Rb}/^{86}\text{Sr}$ ,  $^{147}\text{Sm}/^{144}\text{Nd}$ , and  $^{176}\text{Lu}/^{177}\text{Hf}$  source compositions of shergottites (Fig. 2). In this model, enriched and depleted shergottites plot at opposite ends of the mixing curve. Lunar KREEP and lunar mafic

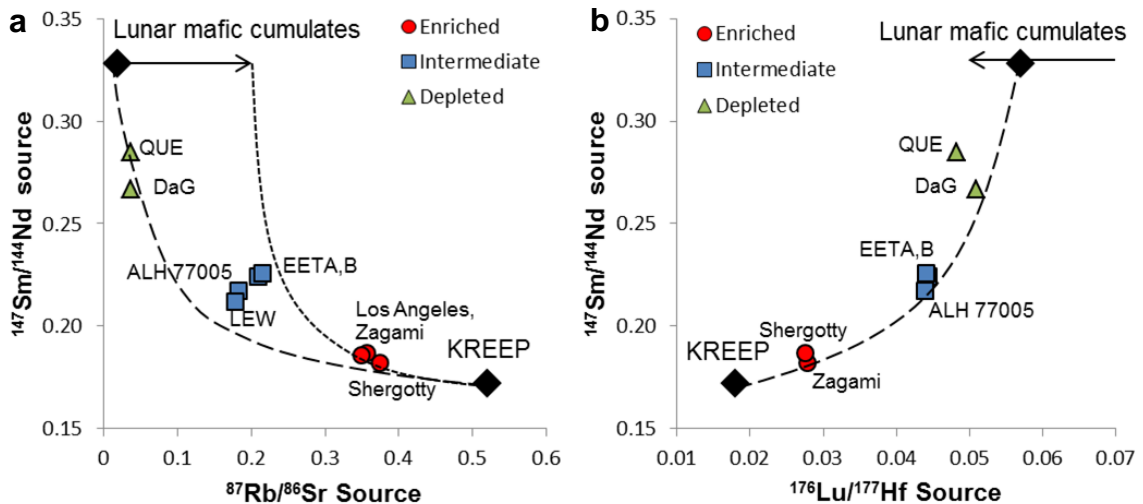


**Fig. 2.** Mixing curves for calculated source compositions for Martian meteorites. Dashed line represents binary mixing curve between the meteorites (Borg et al., 2003). Lunar KREEP-rich and mafic cumulates represent enriched and depleted end-member compositions.  $^{176}\text{Lu}/^{177}\text{Hf}$  and  $^{147}\text{Sm}/^{144}\text{Nd}$  source ratios from Blichert-Toft et al. (1999), Borg et al. (1997; 2002; 2003), Debaille et al. (2008), Nyquist et al. (1979; 1995; 2000), Snyder et al. (1992), Warren and Wasson (1979), and Wooden et al. (1982). Abbreviations for meteorites are QUE = Queen Alexandria 94201, DaG = Dar al Gani 496, EETA,B = EET79001 lithologies A and B, ALH/LEW = Allan Hills 77005, and LA1 = Los Angeles. Modified from Borg et al. (2003).

cumulates were used as end-members for this mixing curve. Since volatile element abundances are different between Mars and the Moon, the Rb concentrations in the lunar sources have been increased by a factor of ~2 to compensate for the variation. In Fig. 2a, the shergottites show an inverse relationship between  $^{147}\text{Sm}/^{144}\text{Nd}$  and  $^{87}\text{Rb}/^{86}\text{Sr}$  source composition. Intermediate shergottite EET A79001 lithologies A and B plot above the mixing line. This suggests that this meteorite must have a different source composition from the other meteorites and that the mixing line should move accordingly. In Fig. 2b, the  $^{147}\text{Sm}/^{144}\text{Nd}$  and  $^{176}\text{Lu}/^{177}\text{Hf}$  source compositions correlate well among the shergottites.

Lapen et al. (2010) adjusted this binary mixing line for the  $^{147}\text{Sm}/^{144}\text{Nd}$  and  $^{176}\text{Lu}/^{177}\text{Hf}$  source compositions by constraining the enriched end-member. They determined that Allan Hills 84001 (ALH 84001), a Martian orthopyroxene cumulate, is a better representation of the enriched end-member compositions than lunar KREEP. Fig. 3 shows the new representation of the mixing curve compared to the one in Borg et al. (2003). The new curve is a better fit for the shergottites.

The purpose of this study is to determine how Tissint is related to other known shergottites in composition, age, and source compositions.

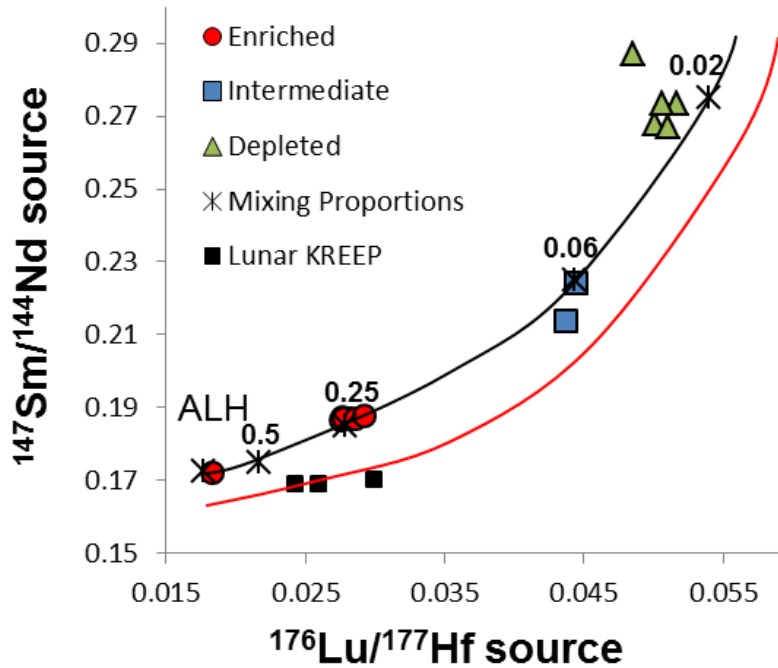


**Fig. 3.** Mixing diagram for  $^{147}\text{Sm}/^{144}\text{Nd}$  and  $^{176}\text{Lu}/^{177}\text{Hf}$  source compositions of shergottites and orthopyroxenite ALH84001. Black squares are KREEP-rich lunar basalts used in the Borg et al. (2003) model. The red line is the binary mixing curve presented by Borg et al. (2003). The black line represents the adjusted mixing curve with fractions of residual trapped liquid marked by a black star modeled by Lapen et al. (2010). Isotope data from Borg et al. (1997; 2003), Blichert-Toft et al. (1999), Bouvier et al. (2005; 2008b), Debaille et al. (2007; 2008), Lapen et al. (2009; 2010), and Shih et al. (2009). Modified from Lapen et al. (2010).

## CHAPTER 2

### Sample Descriptions

Tissint was found as fragments in the desert of Morocco in late 2011. The larger fragments have black fusion crusts and exhibit no evidence of terrestrial weathering. The interior of the fragments reveal an olivine-phyric texture. Olivine macrocrysts (up to 2 mm in diameter) and microphenocrysts are set in a fine-grained groundmass composed of plagioclase (maskelynite), pyroxene (pigeonite and augite), oxides (chromite, ilmenite, magnetite, and pyrrhotite), and phosphate (Chennaoui Aoudjehane et al., 2012; Irving et al., 2012). Petrographic analyses by Chennaoui Aoudjehane et al. (2012), Lin et al. (2012), Stephen et al. (2013), and Udry et al. (2013) show that Tissint is composed of 46-55% pyroxene, 16-28% olivine, 17-24% maskelynite, 1-4% oxides, and 0-2% phosphate. Olivine and pyroxene show chemical zoning in many samples; the rims of the olivine phenocrysts tend to be richer in Fe than the cores, and pyroxenes

tend to have more Ca- and Fe-rich rims than the cores (Chennaoui Aoudjehane et al., 2012; Irving et al., 2012).

The first sample analyzed in this study was a polished thick section (1.65 cm x 1.60 cm x 1 mm) of an interior piece of Tissint. Fig. 4a is a backscatter image of the sample obtained from the JEOL JSM-7600F field emission scanning electron microprobe at NASA Johnson Space Center, Houston, Texas. The porphyritic texture is easily observed in this image. Macrophenocrysts of olivine, up to ~0.4 cm in size, are highly fractured with some grains containing glass pockets (Fig. 4b). Fig. 4c shows the pyroxene, plagioclase, and oxides that constitute the fine-grained groundmass. The grain sizes for pyroxene and plagioclase range from 50 - 200  $\mu\text{m}$ , and the grain size range for oxides is 10 - 30  $\mu\text{m}$ . Fractures are present in the pyroxene whereas plagioclase exhibits no fractures likely due to its conversion to maskelynite.

The second and third samples analyzed in this study consisted of a 1.048 g piece of the interior of Tissint and a whole rock powder, respectively. The interior piece was light gray in color, similar to the interior shown in Fig. 1b, and primarily composed of the fine-grained groundmass with no noticeable olivine phenocrysts. A small glass pocket approximately 100  $\mu\text{m}$  x 350  $\mu\text{m}$  in size on the surface was observed at the center of the sample. During sample preparation, the interior piece was disaggregated and mineral fractions were cleaned using tweezers under a binocular microscope to ensure the fragments of glass were not analyzed.

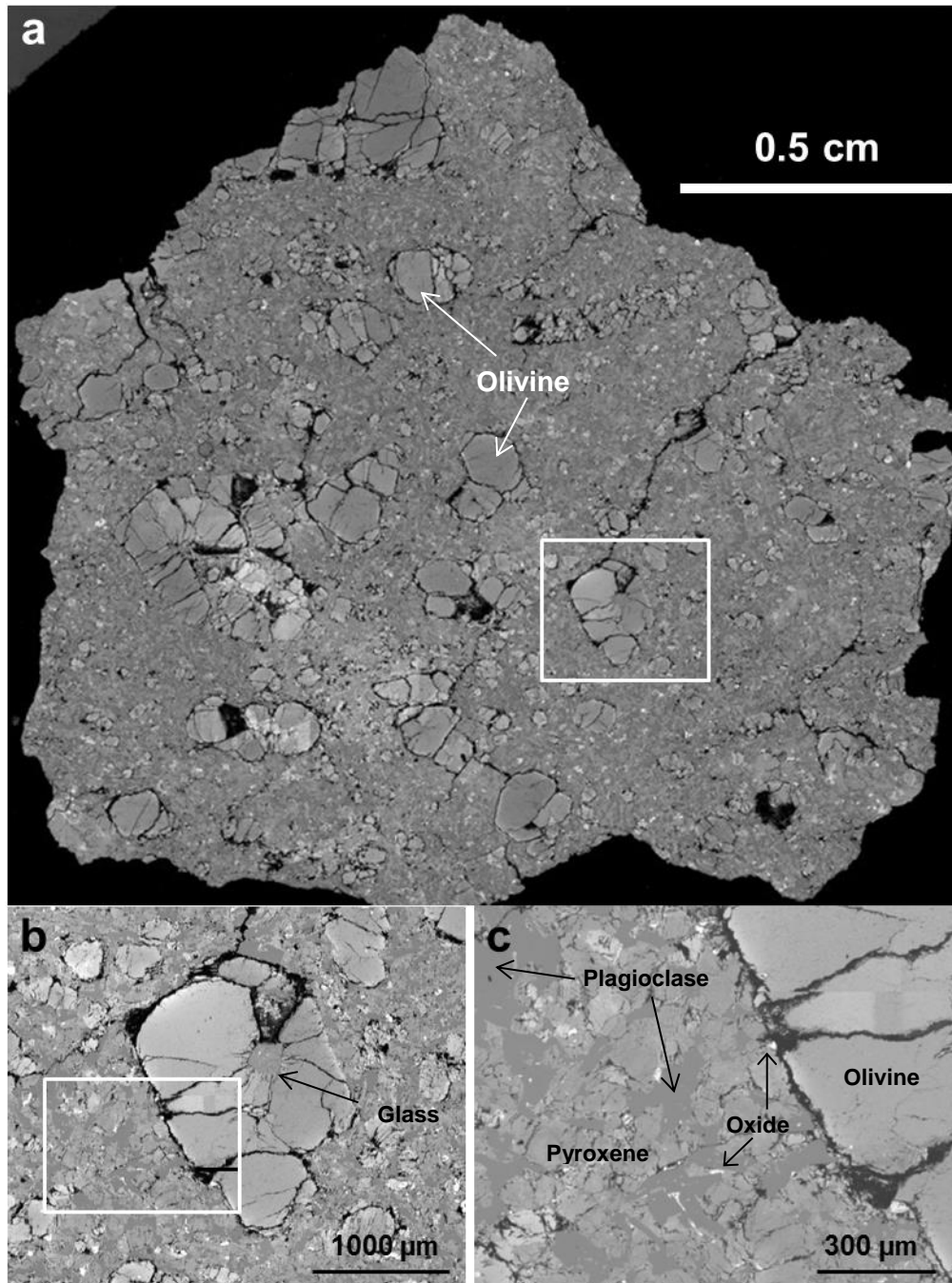


**Fig. 4.** Backscatter image of a thick section of Tissint using a JEOL JSM-7600F FE-SEM. a) Full image of sample b) Inset of a showing an olivine phenocrysts with a preserved glass pocket. c) Inset of b showing fine-grained groundmass containing plagioclase (dark gray), pyroxene (light to medium gray) and oxides (white).

# CHAPTER 3

## Methods

### 3.1 Thick section

#### 3.1.1 Scanning Electron Microscope (SEM)

The polished thick section was carbon coated and attached to a sample holder by carbon tape in preparation for running on the scanning electron microscope and electron microprobe. This sample contained microfractures that resulted in occasional charging during analysis. To reduce the amount of charging, a thicker than standard carbon coat was used as well as additional carbon tape to aid in the conductivity of the sample.

A backscatter image was obtained using the JEOL JSM-7600F Field Emission Scanning Electron Microscope at NASA Johnson Space Center. This image was used to identify and locate olivine, pyroxene, plagioclase, oxide, and phosphate phases for the electron probe micro analyses and *in-situ* analyses by laser ablation inductively coupled plasma mass spectrometer.

### 3.1.2 Electron Probe Micro Analyses (EPMA)

The major constituent phases of Tissint were analyzed for major element compositions using the Cameca SX-100 electron microprobe at the NASA Johnson Space Center, Houston, Texas. Before analyzing the phases in Tissint, the electron microprobe was calibrated using silicate and oxide mineral standards for olivine, pyroxene, plagioclase, and oxide analyses. Silicate, element, and phosphate mineral standards were used for calibration for phosphate analyses. Silicate and oxide phases were analyzed using a 15 kV accelerating voltage, 20 nA beam current, and a 1  $\mu\text{m}$  beam size. Phosphates were analyzed using a 15 kV accelerating voltage, 10 nA beam current, and a 5  $\mu\text{m}$  beam size.

Element data are reported as weight percent oxides of the major elements and only analyses with total weight percent between 98% and 102% are used in this study. Few exceptions were made to this criterion when weight percent oxides remained within the ranges measured for similar compositions. The number of analyses used for each phase are as follows: olivine – 37, pyroxene – 86, plagioclase – 37, oxides – 30, and phosphates – 6. Due to the presence of fractures in the olivine, olivine analyses did not provide acceptable data for core to rim compositional analyses.

### 3.1.3 Laser Ablation Inductively Coupled Plasma Mass Spectrometry (LA-ICP-MS)

Trace element abundances of the major constituent phases were measured *in-situ* by LA-ICP-MS at the University of Houston, Houston, Texas, using a Varian 810 quadrupole mass spectrometer coupled with a PhotonMachines Analyte.193 excimer laser ablation system. *In-situ* analyses were performed on olivine, pyroxene, and plagioclase using a 50  $\mu\text{m}$  diameter laser spot size with a 7 Hz repetition rate over 20 s and a fluence of 3 J/cm<sup>2</sup>. A 25  $\mu\text{m}$  diameter laser spot size was used for oxide analysis.

Trace element concentrations were calculated using the *Glitter* data reduction software. The REE concentrations for the major constituent phases determined from *in situ* analyses are normalized to CHUR values (Anders and Grevesse, 1989) and compared with bulk analyses for Tissint and other depleted shergottites. The concentrations for Lu, Hf, Sm, and Nd in pyroxene, plagioclase, and oxides are used to estimate the amounts of mixed  $^{176}\text{Lu}$ - $^{178}\text{Hf}$  and  $^{149}\text{Sm}$ - $^{150}\text{Nd}$  spikes needed for each aliquot.

### **3.2 Interior Sample and Whole Rock Powder**

#### *3.2.1 Sample Preparation*

A 1.048 g interior piece of a Tissint fragment was crushed using a boron carbide mortar and pestle. Next, the grains were sieved into three size fractions using 100 mesh, 200 mesh, and 325 mesh screens. The grains smaller than 325 mesh were analyzed as a whole rock fraction (WR1). The separate whole rock powder (WR2) was already crushed and does not undergo any sample preparation prior to sample digestion.

Heavy liquids were used to separate the minerals for the 100-200 mesh and 200-325 mesh size fractions. Acetylene tetra-bromide was used to separate phases above and below a density of 2.85 g/cc. In general, this liquid is used to separate the plagioclase from the denser olivine, pyroxene, and oxide minerals. To separate the oxides from the pyroxene and olivine, thallium malonate formate with a density of 4.0 g/cc was used.

For the heavy-liquid separation process, the grains are put in a 1.5 ml centrifuge tube with 700  $\mu\text{l}$  of the heavy liquid and centrifuged for about two minutes. The less-dense minerals float on top of the liquid whereas the minerals denser than the liquid sink

to the bottom of the centrifuge tube. The bottom of the centrifuge tube is placed in liquid nitrogen to freeze the liquid to keep the minerals from mixing during transfer from the tube to a glass beaker. The non-frozen mineral fraction is transferred to a beaker and the heavy liquid is removed by rinsing the grains with a soluble liquid. This rinsing process lowers the density of heavy liquid and allows the heavy liquid to separate from the grains. Acetylene tetra-bromide is soluble with acetone and thallium malonate is soluble with water. The heavy liquid is removed by pouring the heavy liquid and soluble liquid into the appropriate waste container. The cleaned grains are transferred to a petri dish and set to dry. The cleaning process is repeated for the denser minerals when they become unfrozen. The heavy liquid separation process resulted in plagioclase, pyroxene and olivine, and oxide fractions in both 100 - 200 mesh and 200 - 325 mesh size fractions.

The next step was to purify the mineral separates. Although the heavy liquid separation process is helpful in separation the mineral phases, some grains will still have other phases attached. For example, some plagioclase grains will contain pyroxene or oxide within the grain. To ensure the purest grains are used for analysis, each mineral fraction was “cleaned” under a binocular microscope using tweezers. Since pyroxene and olivine were separated into the same fractions due to similar densities, the entire amount of pyroxene used for analysis was picked using the binocular microscope and tweezers. Olivine was not separated for analysis because the REE concentrations were below detection limits using LA-ICP-MS.

### *3.2.2 Sample Digestion*

The digestion process converts the solid sample into a solution in preparation for column chemistry. Each sample is weighed and put in a Savillex<sup>®</sup> beaker. The weights measured prior to digestion are as follows: plagioclase - 38.05 mg, pyroxene - 35.44 mg,

oxides - 1.45 mg, and whole rock fraction (WR1) - 29.27 mg. The whole-rock powder (WR2) sample weighed out to 114.82 mg and was run through the same chemistry process at a separate time from the other samples. Amounts of mixed  $^{176}\text{Lu}$ - $^{178}\text{Hf}$  and  $^{149}\text{Sm}$ - $^{150}\text{Nd}$  spikes that were estimated from LA-ICP-MS data and sample weights were added to each sample and a procedural blank. The samples were dissolved in 0.5 ml twice distilled (2x)  $\text{HNO}_3$  and 2 ml 2x 29M HF for 24 hours at  $100^\circ\text{C}$ . The samples were dried on a hotplate and brought back up in 0.5 ml 2x  $\text{HNO}_3$  and 4 ml 2x 29M HF. Next, the samples were transferred to PTFE Teflon Parr™ bomb liners and steel jackets and placed in the oven at  $150^\circ\text{C}$  for 48 hours. After the bombs were cooled, the samples were transferred back into their original Savillex® beakers and dried on a hotplate. The samples were further dissolved in 2 ml 2x 6M  $\text{HNO}_3$  or 1 ml once distilled (1x) 6M HCl until the entire solution was clear of any fluoride salts after centrifuging. The oxide and WR1 cuts appeared to have oxide grains present after the first dissolution procedure. For these samples (including a blank), the bombing procedure was repeated for another 30 hours. Any chromite grains that remained after this step were finally removed from the solution by centrifuge prior to column chemistry.

### *3.2.3 Ion-exchange chromatography*

The digested samples were run through four sets of ion-exchange columns to isolate Lu, Hf, Sm, and Nd following procedures outlined in Lapen et al. (2004; 2010). The first set of columns uses DOWEX 1x8-200 mesh resin and 6M HCl to remove Fe from the samples. The second set of columns uses cation Eichrom Ln-spec resin. REE and major elements are collected after the samples are loaded on the resin by passing 6M HCl. Ti and Zr are removed using a recipe containing citric acid. Lastly, Hf is collected with 6M HCl-0.2 M HF. Next, the REE and major element cuts are loaded into the third set of columns. These columns use Eichrom RE-spec resin and 4.5M HCl to extract the

REE from the solution. The final set of columns use a cation resin converted to  $\text{NH}_4^+$  form along with  $\alpha$ -hydroxy-isobutaic (HIBA) acid. Lu, Sm, and Nd are collected from this set of columns using 0.15M  $\alpha$ -HIBA and 0.21M  $\alpha$ -HIBA acid. After the samples are dried, 50  $\mu\text{l}$  2x  $\text{HNO}_3$  concentrate are added to each sample and dried. This step prepares the sample for isotope analysis by converting the acid in the sample to  $\text{HNO}_3$ .

#### *3.2.4 Multi-collector Inductively Coupled Mass Spectrometry (MC-ICP-MS)*

All Hf, Nd, Sm, and Lu fractions from each sample were analyzed on the NuPlasma II MC-ICP-MS using a Cetac Aridus II nebulizer at the University of Houston, Houston, Texas. The Hf samples were brought up in 1 ml 2%  $\text{HNO}_3$ -1% HF and the Lu, Sm, and Nd samples were brought up in 800 ml 2%  $\text{HNO}_3$  in preparation for isotope analysis. After the samples were dissolved, a pre-concentration test was run on all samples. 20  $\mu\text{l}$  of the Hf solutions and 10  $\mu\text{l}$  of the Lu, Sm, and Nd solutions were diluted in 500  $\mu\text{l}$  of 2%  $\text{HNO}_3$ -1% HF and 2%  $\text{HNO}_3$ , respectively, and were analyzed on the MC-ICP-MS. Based on the pre-concentration test, each sample was diluted to a desired concentration for the normal analysis.

The Hf samples that were analyzed on the MC-ICP-MS were diluted to 25 ppb or analyzed at full concentration. Hf samples are mass-bias corrected and spike subtracted following the method outlined in Lapen et al. (2004). This method uses “a linear instrumental mass-bias coefficient relative to the accepted true values of the [bracketing] standards.” The bracketing samples are interspersed between the samples and are UH JMC 475 Hf 25 ppb, UH AMES 475 Hf 25 ppb, and UWisc JMC 475 Hf 25 ppb. The isobaric inferences of  $^{176}\text{Lu}$  and  $^{176}\text{Yb}$  on  $^{176}\text{Hf}$  and  $^{180}\text{W}$  and  $^{180}\text{Ta}$  on  $^{180}\text{Hf}$  were corrected by following procedures outlined in Lapen et al. (2004).

The  $^{176}\text{Hf}/^{177}\text{Hf}$  operating values measured for internal laboratory standards during run 1 (samples 12HN102, 12HN103, 12HN104, and 12HN105) are UH JMC 475

Hf 25 ppb  $0.282196 \pm 0.000067$  ( $2\sigma$ ,  $n = 21$ ), UH AMES 475 Hf 25 ppb  $0.282355 \pm 0.000053$  ( $2\sigma$ ,  $n = 5$ ), and UWisconsin JMC 475 (identical to the original USGS JMC-475 standard) Hf 25 ppb  $0.282154 \pm 0.000054$  ( $2\sigma$ ,  $n = 7$ ); and run 2 (sample 12NH4) are UH JMC 475 Hf 36 ppb  $0.282196 \pm 0.000016$  ( $2\sigma$ ,  $n = 9$ ) and UWisconsin JMC 475 Hf 36 ppb  $0.282153 \pm 0.000016$  ( $2\sigma$ ,  $n = 5$ ).

All Lu samples were run at full concentration because I expected low concentration values ( $\sim < 20$  ppm) from the pre-concentration check. The isobaric interferences of  $^{174}\text{Hf}$  on  $^{174}\text{Yb}$ ,  $^{176}\text{Hf}$  and  $^{176}\text{Yb}$  on  $^{176}\text{Lu}$ , and  $^{180}\text{W} + ^{180}\text{Ta}$  on  $^{180}\text{Hf}$  were corrected for along with mass bias corrections for  $^{175}\text{Lu}/^{176}\text{Lu}$  ratios by following methods outlined in Vervoort et al. (2004).

The Nd and Sm analyses methods are similar to those of the Hf and Lu methods described above. The Nd samples were diluted to 10 ppb, 40 ppb, or run at full concentration. The  $^{143}\text{Nd}/^{144}\text{Nd}$  operating values measured for internal laboratory standards during run 1 are UH AMES Nd 40 ppb  $0.511972 \pm 0.000017$  ( $2\sigma$ ,  $n = 39$ ), UH AMES Nd 10 ppb  $0.511992 \pm 0.000038$  ( $2\sigma$ ,  $n = 3$ ), UH AMES Nd 500 ppt  $0.511675 \pm 0.000898$  ( $2\sigma$ ,  $n = 4$ ), JNdi Nd UH 40 ppb  $0.512102 \pm 0.000019$  ( $2\sigma$ ,  $n = 6$ ), JNdi Nd UH 10 ppb  $0.512085 \pm 0.000055$  ( $2\sigma$ ,  $n = 4$ ), and JNdi Nd UH 500 ppt  $0.511777 \pm 0.000695$  ( $2\sigma$ ,  $n = 4$ ), and run 2 are JNdi Nd UH 150 ppb  $0.512103 \pm 0.00004$  ( $2\sigma$ ,  $n = 13$ ) and JNdi Nd UH 40 ppb  $0.512092 \pm 0.00008$  ( $2\sigma$ ,  $n = 4$ ). Sm samples were diluted to 20 ppb or run at full concentration for those below 20 ppb. Isobaric interferences for  $^{142}\text{Ce}$ ,  $^{144}\text{Sm}$ ,  $^{148}\text{Sm}$ , and  $^{150}\text{Sm}$  on Nd and  $^{144}\text{Nd}$ ,  $^{148}\text{Nd}$ ,  $^{150}\text{Nd}$ ,  $^{152}\text{Gd}$ , and  $^{154}\text{Gd}$  on Sm were corrected for along with instrumental mass bias following methods outlined in Lapen et al. (2004).

# CHAPTER 4

## Results

### 4.1 Electron Probe Microanalyses

The representative composition for major elements of pyroxene, olivine, plagioclase, oxides, and phosphates are listed in Tables 1 and 2. The oxide weight percent values are from the raw data of the microprobe analyses, however, weight percent values for FeO and Fe<sub>2</sub>O<sub>3</sub> for oxides were calculated by stoichiometry using Droop (1987).

Calculations of the chemical formulas and end-member compositions follow the methods outlined in Deer et al. (1992).

Eighty-six analyses were done on 20 pyroxene grains and they indicate pigeonite (72 analyses), augite (9), and orthopyroxene (5) occur in this sample. Table 1 lists the representative compositions for the pyroxenes and Fig. 5a shows the compositional variations of the analyses plotted on the pyroxene quadrilateral diagram. Pigeonite is the dominant pyroxene measured with orthopyroxene and augite, which are present in

lower abundances. Although orthopyroxene and augite are present in small abundances, their occurrences within the sample are distinct. Orthopyroxene was measured in the core of two grains with zoning to pigeonite in the rims of these grains, and augite compositions were located adjacent to plagioclase grains.

The representative compositions for olivine and the macrocryst olivine cores are presented in Table 1, and the end-member compositional range is shown in Fig. 5b. The olivine composition ranges from  $Fo_{39.2}$  –  $Fo_{81.4}$  indicating the olivine is Mg-rich. These values are consistent with those measured for olivine cores by Irving and Kuehner (2012) with the most Mg-rich value being  $Fo_{81.4}$ .

The representative composition for plagioclase is presented in Table 1. The end-member compositional range represented in Fig. 5c and shows that plagioclase in Tissint is Ca-rich with a compositional range from  $An_{49.9}$  to  $An_{72.3}$ . This range in association with the Fe/Mn values for pyroxene (63, 64, and 74) and olivine (56) are consistent with the anorthite and Fe/Mn ranges for Mars determined by Papike et al. (2003).

From 30 analyses, three oxide constituents were determined from the raw microprobe data. These three constituents are ilmenite (~50 wt%  $TiO_2$ , <1 wt%  $Cr_2O_3$ , and 42-46 wt%  $FeO_T$ ; where  $FeO_T$  is total Fe expressed as FeO), chromite (<7% wt%  $TiO_2$ , >37% wt%  $Cr_2O_3$ , and 28-41 wt%  $FeO_T$ ), and titanomagnetite (22-27 wt%  $TiO_2$ , 2-17 wt%  $Cr_2O_3$ , and 52-63 wt%  $FeO_T$ ). The dominant oxide composition analyzed was titanomagnetite. These oxide grains are found between grains of plagioclase and pyroxene, except for one chromite grain which was found as an inclusion in an olivine phenocryst.

**Table 1.** Representative compositions for pyroxene, olivine, and plagioclase.

	Pigeonite	Augite	Orthopyroxene	Olivine	Olivine Core	Plagioclase
Oxide wt%						
SiO <sub>2</sub>	52.3	50.3	54.1	37.0	39.8	54.6
TiO <sub>2</sub>	0.18	0.45	0.12	0.02	0.02	-----
Al <sub>2</sub> O <sub>3</sub>	1.09	1.91	0.82	0.09	0.06	28.7
Cr <sub>2</sub> O <sub>3</sub>	0.43	0.61	0.49	0.06	0.19	-----
FeO*	19.3	16.7	17.0	37.0	17.5	0.66
MnO	0.62	0.56	0.58	0.73	0.35	-----
MgO	19.8	15.4	24.7	26.2	50.0	0.12
CaO	5.88	13.4	2.34	0.31	0.24	12.3
Na <sub>2</sub> O	0.08	0.13	0.04	<0.01	0.01	4.18
K <sub>2</sub> O	0.02	<0.01	<0.01	<0.01	<0.01	0.09
BaO	-----	-----	-----	-----	-----	<0.01
Total	99.7	99.43	100.2	98.97	101.05	100.7
Si	1.963	1.918	1.969	0.984	1.610	2.440
<sup>IV</sup> Al	0.048	0.082	0.025	0.003	0.002	1.509
<sup>VI</sup> Al	0.012	0.005	0.004	-----	-----	-----
Fe <sup>3+</sup>	0.013	0.063	0.046	-----	-----	-----
Ti	0.005	0.013	0.003	<0.001	<0.001	-----
Cr	0.013	0.018	0.014	0.001	0.004	-----
Mg	1.107	0.876	1.397	1.114	1.610	0.008
Fe <sup>2+</sup>	0.592	0.470	0.464	0.883	0.367	0.049
Mn	0.020	0.018	0.017	0.018	0.008	-----
Ca	0.236	0.549	0.086	0.009	0.006	0.590
Na	0.006	0.010	0.002	<0.001	0.001	0.362
K	0.001	<0.001	<0.001	<0.001	0.002	0.005
Total cation	4.004	4.021	4.008	3.013	2.998	4.964
Mg#	65	62	74	56	81	-----
Fe/Mn	31	30	28	50	49	-----
Cr#	21	18	33	-----	-----	-----
Fo	-----	-----	-----	56	81	-----
Wo/An	12.1	27.8	4.65	-----	-----	61.6
Fs/Ab	31.7	27.9	27.3	-----	-----	37.8
En/Or	56.2	44.3	68.1	-----	-----	0.53

Notes: Cation and end-member calculations following methods outlined in Deer et al. (1992). Estimation of Fe<sup>3+</sup> determined using Droop (1987). Mineral formula normalization for pyroxene, olivine, and plagioclase are 6, 4, and 8 oxygens, respectively.

\*FeO = FeO + Fe<sub>2</sub>O<sub>3</sub>

**Table 2.** Representative compositions for oxides and phosphates.

	Ilmenite	Chromite	Titano- magnetite		Phosphates
Oxide wt%				SiO <sub>2</sub>	1.59
SiO <sub>2</sub>	0.19	0.01	0.10	Al <sub>2</sub> O <sub>3</sub>	0.39
TiO <sub>2</sub>	49.9	0.70	23.0	FeO	2.95
Al <sub>2</sub> O <sub>3</sub>	0.17	8.61	3.66	MnO	0.15
Cr <sub>2</sub> O <sub>3</sub>	0.41	56.2	15.8	MgO	2.38
FeO	41.4	26.1	50.2	CaO	46.1
Fe <sub>2</sub> O <sub>3</sub>	3.93	1.65	3.64	Na <sub>2</sub> O	1.04
MnO	0.73	0.49	0.64	K <sub>2</sub> O	0.11
MgO	1.56	4.86	1.77	P <sub>2</sub> O <sub>5</sub>	43.9
CaO	0.19	0.03	0.04	La <sub>2</sub> O <sub>3</sub>	<0.01
V <sub>2</sub> O <sub>3</sub>	2.45	0.49	1.58	Ce <sub>2</sub> O <sub>3</sub>	<0.01
Na <sub>2</sub> O	<0.01	0.01	0.01	F	0.20
K <sub>2</sub> O	<0.01	<0.01	<0.01	Cl	0.02
Total	101.0	99.36	100.4	Total	98.9
Si	0.003	0.008	0.004	Si	0.289
Al	0.005	0.352	0.155	Al	0.084
Fe <sup>3+</sup>	0.073	0.043	0.099	Fe <sup>2+</sup>	0.448
Fe <sup>2+</sup>	0.854	0.758	1.509	Mg	0.643
Ti	0.928	0.018	0.622	Mn	0.023
Cr	0.008	1.540	0.449	Ca	8.982
Mg	0.058	0.251	0.095	Na	0.368
Mn	0.015	0.014	0.019	K	0.024
Ca	0.005	0.001	0.002	P	6.753
V	0.049	0.014	0.046	La	<0.001
Na	<0.001	0.001	0.001	Ce	<0.001
K	<0.001	<0.001	<0.001	F	0.115
Total cation	2.000	3.000	3.000	Cl	0.006
				Total cation	17.61
Mg#	5.9	24	5.6		
Fe/Mn	61	55	83		
Cr#	62	81	74		
Chr	-----	78.1	23.1		
Mt	-----	2.19	5.09		
Sp	-----	17.9	7.97		
Usp	-----	1.85	63.9		

Notes: Cation calculations following methods outlined in Deer et al. (1992). End-member calculations following Gross et al. (2011). Estimation of Fe<sup>3+</sup> and new weight percent of FeO and Fe<sub>2</sub>O<sub>3</sub> determined using Droop (1987). Ilmenite normalized to 3 oxygens. Chromite and titanomagnetite are normalized to 4 oxygens. Phosphates are normalized to 28 oxygens.

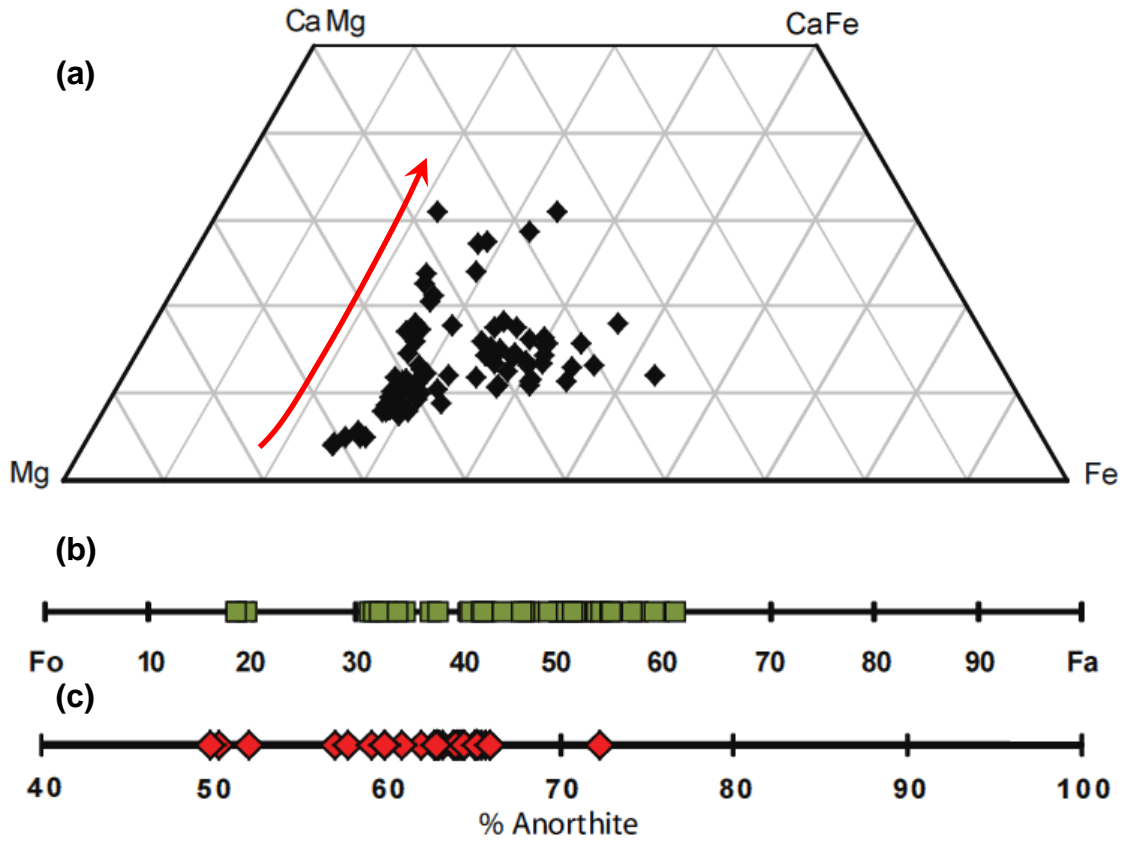


**Fig. 5.** Elemental compositions of the major constituent phases. All analyses were measured using the Cameca SX-70 electron microprobe at NASA Johnson Space Center. To ensure high-quality EMP data, the analyses above measured total oxide weight percents between 98 and 102. (a) Pyroxene composition based on 86 analyses. The red arrow represents the crystallization trend discussed in chapter 5, (b) Olivine composition based on 37 analyses, (c) Plagioclase composition based on 37 analyses.

#### 4.2 REE Concentrations

The average chondrite-normalized REE concentrations of the primary phases and bulk rock are represented in Fig. 6. Bulk rock abundances for other depleted shergottites are also plotted for comparison of REE patterns. Concentrations of most REE in olivine were below the detection limits of the LA-ICP-MS and, therefore, are not plotted in the diagram. Based on these low REE concentrations in olivine, it was not analyzed for isotopic compositions for the Lu-Hf and Sm-Nd isochrons. REE concentrations measured in this study are represented in Appendix 1.

*In-situ* trace-element analyses of plagioclase and pyroxene show similar REE patterns to bulk Tissint and other depleted shergottites. The bulk rock and mineral compositions show depletion in LREE with an increasing slope from LREE to middle REE and a moderately flat pattern from the middle to HREE elements. A high positive Eu anomaly is observed in plagioclase whereas pyroxene exhibits a low to moderate negative Eu anomaly.

The abundances measured *in-situ* for plagioclase and pyroxene show differences from those measured using the MC-ICP-MS during isotope analysis. The abundances for Lu, Hf, Sm, and Nd measured using the MC-ICP-MS are presented in Tables 3 and 4. The Lu abundance measured *in-situ* is approximately ten times greater than that measured on the multi-collector ICP-MS. The Nd abundance measured using MC-ICP-MS is approximately 5 times greater than that measured *in-situ*. These variations in measured abundances are likely due to “dirty” grains in the mineral fractions. The steep slope for LREE of plagioclase and difference in the measurement of the abundances in Lu, Hf, Sm, and Nd may indicate mixed phase analyses. The Sm abundances measured *in-situ* for pyroxene are approximately 4.5 times greater than measured on the multi-collector. The Lu, Hf, and Nd abundances were similar between to two methods for the pyroxene indicating little mixing of phases during *in-situ* analysis.

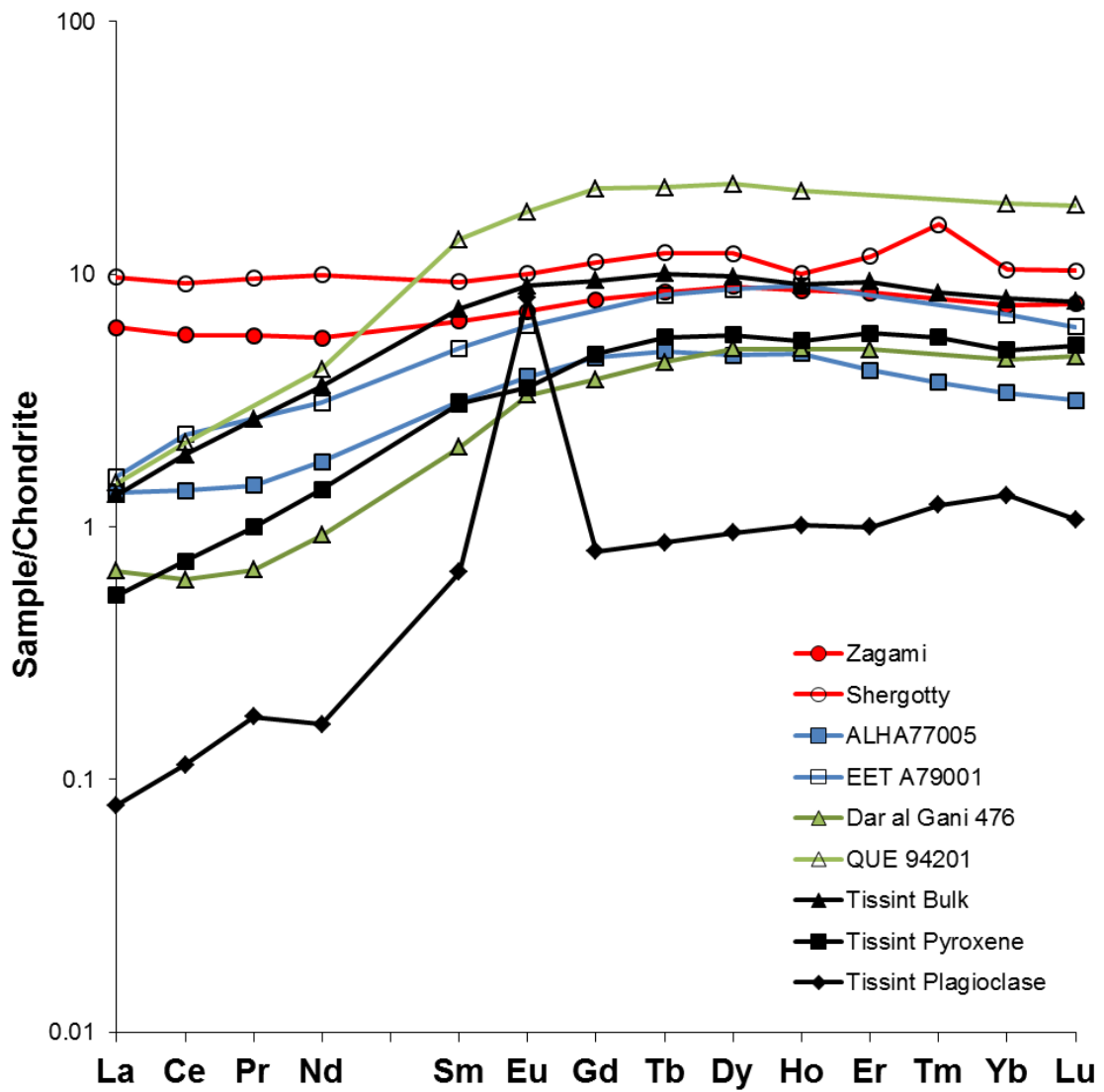


**Fig. 6.** Chondrite normalized REE abundances for Tissint phases (this study), bulk Tissint, and other depleted shergottites. Bulk rock abundance data from Dreibus et al. (1982; 1996), Burghelle et al. (1983), Smith and Steele (1994), Barrat et al. (2001), Irving et al. (2012), and Chennaoui Aoudjehane et al. (2012). Normalized to chondrite values from Anders and Grevesse (1989).

### 4.3 Lu-Hf and Sm Nd Isochrons

The crystallization ages for the sample were calculated from the internal isochron lines formed by the compositions of the mineral separates. The equation to calculate the crystallization age (T) is as follows:

$$T = \frac{1}{\lambda} \ln \left[ 1 + \frac{(daughter\ ratio)_{sample} - (daughter\ ratio)_{initial}}{(parent\ ratio)_{sample}} \right] \quad (\text{Equation 1})$$

where  $\lambda$  is the decay constant and the initial daughter ratio is the y-intercept of the isochron. The decay constants used for all calculations are  $1.865 \times 10^{-11} \text{ a}^{-1}$  for  $^{176}\text{Lu}$ - $^{176}\text{Hf}$  and  $6.54 \times 10^{-12} \text{ a}^{-1}$  for  $^{147}\text{Sm}$ - $^{143}\text{Nd}$  (Scherer et al., 2001; Faure and Mensing, 2005).

Initial  $\epsilon^{176}\text{Hf}$  and  $\epsilon^{143}\text{Nd}$  are values that express the enrichment of the source relative to CHUR at the time of crystallization. These values were calculated using equations 2 and 3 (Faure and Mensing, 2005).

$$\epsilon Hf_i = \left[ \frac{(^{176}\text{Hf}/^{177}\text{Hf})_{sample}}{(^{176}\text{Hf}/^{177}\text{Hf})_{CHUR}} - 1 \right] * 10^4 \quad (\text{Equation 2})$$

$$\epsilon Nd_i = \left[ \frac{(^{143}\text{Nd}/^{144}\text{Nd})_{sample}}{(^{143}\text{Nd}/^{144}\text{Nd})_{CHUR}} - 1 \right] * 10^4 \quad (\text{Equation 3})$$

All ratios are calculated to be the ratios at the time of crystallization. Present-day CHUR isotope ratios used in all calculations are  $^{176}\text{Hf}/^{177}\text{Hf} = 0.282785$ ,  $^{176}\text{Lu}/^{177}\text{Lu} = 0.0336$ ,  $^{143}\text{Nd}/^{144}\text{Nd} = 0.512637$ , and  $^{147}\text{Sm}/^{144}\text{Nd} = 0.1964$  (Bouvier et al., 2008a).

#### 4.3.1 $^{176}\text{Lu}$ - $^{176}\text{Hf}$ Isochron

The results for the Lu-Hf isotopic analyses are listed in Table 1 and on an internal isochron defined by the plagioclase, pyroxene, and WR2 fractions in Fig. 7. The  $^{176}\text{Lu}$ - $^{176}\text{Hf}$  isochron yielded a crystallization age of  $570 \pm 84 \text{ Ma}$ , an initial  $^{176}\text{Hf}/^{177}\text{Hf}$  value of  $0.284060 \pm 0.000046$ , and  $\text{MSWD} = 2.4$ . The calculated initial  $\epsilon^{176}\text{Hf}$  using the calculated age and initial ratio is  $+57.9 \pm 2.5$ . A more precise initial  $\epsilon^{176}\text{Hf}$  value of  $+57.8$

$\pm 0.9$  is calculated in Chapter 5 using the weighted average of internal isochron ages and whole rock isotope compositions.

The oxide and WR1 fractions did not plot on the isochron and were, therefore, not used in the calculations for the isochron. Contamination during the preparation process or fractionation during leaching may be the cause of these two fractions plotting off the isochron. Previous work has shown decoupling of Lu and Hf during gentle leaching of fine-grained shergottites is possible (Lapen et al., 2008).

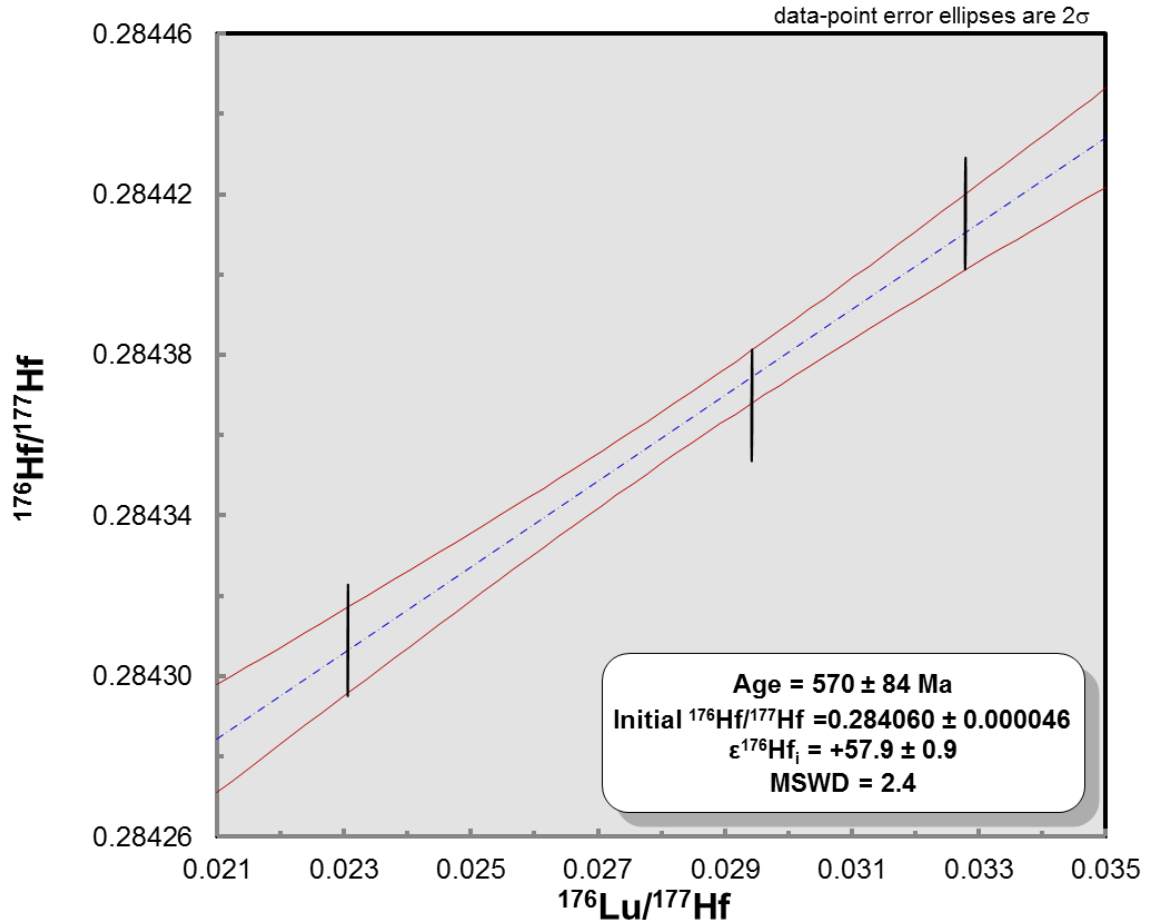


**Fig. 7.** Lu-Hf isochron. Line calculated from plagioclase and pyroxene mineral separates and whole rock 2 (WR2). Age calculated from external reproducibility of standards throughout the Lu and Hf analyses. Red lines represent the error envelope of the isochron. The decay constant used for the  $^{176}\text{Lu}$  isochron and  $\epsilon^{176}\text{Hf}$  is  $1.865 \times 10^{-11} \text{ a}^{-1}$  (Scherer et al., 2001).

**Table 3.** Lu and Hf data for Tissint. Errors displayed are  $\pm 2\sigma$  from measured compositions.

Sample #	Description	Weight (g)	Lu (ppm)	Hf (ppm)	$^{176}\text{Lu}/^{177}\text{Hf}$	$^{176}\text{Hf}/^{177}\text{Hf}$
12HN102	Plagioclase	0.03805	0.115	0.722	0.023060	0.284309 $\pm$ 4
12HN103	Pyroxene	0.03544	0.126	0.559	0.032787	0.284415 $\pm$ 4
12HN104	Oxides	0.00145	0.060	3.453	0.002517	0.283891 $\pm$ 7
12HN105	Whole Rock 1	0.02927	0.187	1.079	0.025178	0.284033 $\pm$ 3
12NH004	Whole Rock 2	0.11482	0.155	0.761	0.0290702	0.284367 $\pm$ 2

#### 4.3.2 $^{147}\text{Sm}$ - $^{143}\text{Nd}$ Isochron

The results for the Sm-Nd isotopic analyses are listed in Table 2 and on an internal isochron defined by the plagioclase, pyroxene, and WR1 fractions in Fig. 8. The  $^{147}\text{Sm}$ - $^{143}\text{Nd}$  isochron yielded a crystallization age of  $690 \pm 140$  Ma, an initial  $^{143}\text{Nd}/^{144}\text{Nd}$  value of  $0.51376 \pm 0.00034$ , and MSWD = 1.3. The calculated initial  $\epsilon^{143}\text{Nd}$  using this age and initial ratio is  $+39.4 \pm 7.5$ . A more precise initial  $\epsilon^{143}\text{Nd}$  value of  $+41.6 \pm 1.5$  is calculated in Chapter 5 using the weighted average of internal isochron ages and whole rock isotope compositions. The Sm and Nd concentrations in the oxide fraction were too low to measure and were not used for the Sm-Nd isochron.

**Table 4.** Sm and Nd data for Tissint. Errors displayed are  $\pm 2\sigma$  from measured compositions.

Sample #	Description	Weight (g)	Sm (ppm)	Nd (ppm)	$^{147}\text{Sm}/^{144}\text{Nd}$	$^{143}\text{Nd}/^{144}\text{Nd}$
12HN102	Plagioclase	0.03805	0.059	1.104	0.363064	$0.515396 \pm 19$
12HN103	Pyroxene	0.03544	2.001	0.822	0.395391	$0.515532 \pm 15$
12HN105	Whole Rock 1	0.02927	1.432	1.520	0.378376	$0.515454 \pm 18$
12NH004	Whole Rock 2	0.11482	0.611	0.625	0.379692	$0.515478 \pm 09$

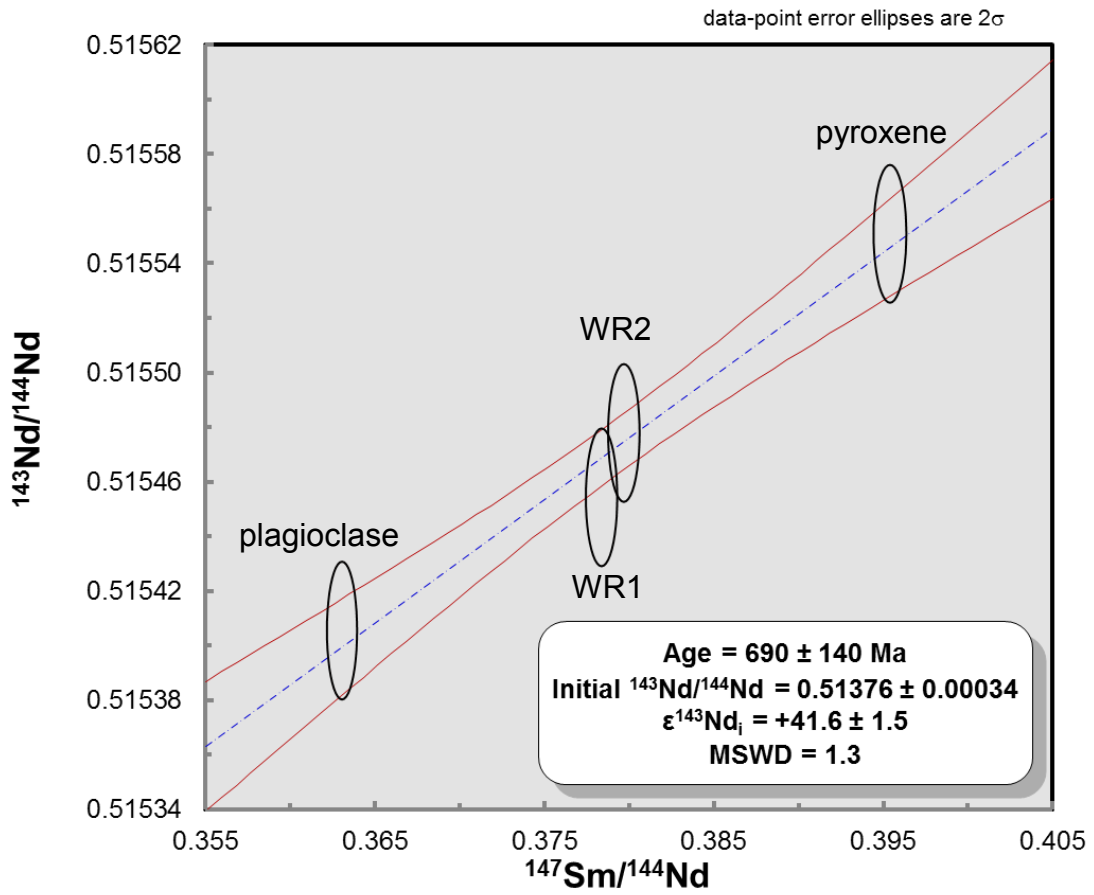


**Fig. 8.** Sm-Nd isochron. Line calculated from plagioclase and pyroxene mineral separates and whole rocks 1 (WR1) and 2 (WR2). Age calculated from external reproducibility of standards throughout the Sm and Nd analyses. Red lines represent the error envelope of the isochron. The decay constant used for the  $^{147}\text{Sm}$  isochron and  $\epsilon^{143}\text{Nd}$  is  $6.54 \times 10^{-12} \text{ a}^{-1}$  (Faure and Mensing, 2005).

# CHAPTER 5

## Discussion

### 5.1 Composition

#### 5.1.1 Pyroxene

The compositions of the 86 pyroxene analyses in this study were plotted on the pyroxene QUAD diagram (Fig. 5a) to identify the crystallization trend of pyroxene in Tissint. Papike et al. (2009) identified similar crystallization trends among several olivine-phyric shergottites, including DaG 476, Sayh al Uhaymir (SaU) 005, and Yamato (Y-) 980459. Their analyses showed distinct trends of initial crystallization of orthopyroxene or pigeonite with zoning to augite for all of the olivine-phyric shergottites they analyzed. The scatter of the pyroxene analyses illustrated in Fig. 5a is similar to that presented by Irving and Kuehner (2012) and indicates there is more variation in the pyroxene composition in Tissint compared to other olivine-phyric shergottites. Although the composition is more variable than other olivine-phyric shergottites, zoning of orthopyroxene to pigeonite and pigeonite to augite was observed in multiple pyroxene

grains in this study and, therefore, the crystallization trend of the other olivine-phyric shergottites can be applied to Tissint. This trend is illustrated by the red arrow in Fig 5a.

Manganese and iron systematics are another useful tool in shergottite identification. Fig. 9 shows a positive correlation of Mn with Fe for pyroxene and olivine in this study. These trends are consistent with other olivine-phyric shergottites (Papike et al., 2009). The Fe/Mn ratios for bulk rock, pyroxene, and olivine are lower in Martian rocks and eucrites (bulk, ~35 and ~40, respectively) relative to Earth and the Moon (bulk, ~60 and 70-75, respectively) (Stolper et al., 1979; Treiman et al., 2000). The average Fe/Mn ratios for pigeonite, augite, and orthopyroxene are 29, 27, and 28, respectively, and are consistent with those determined by Papike et al. (2003) of  $32 \pm 6$ .

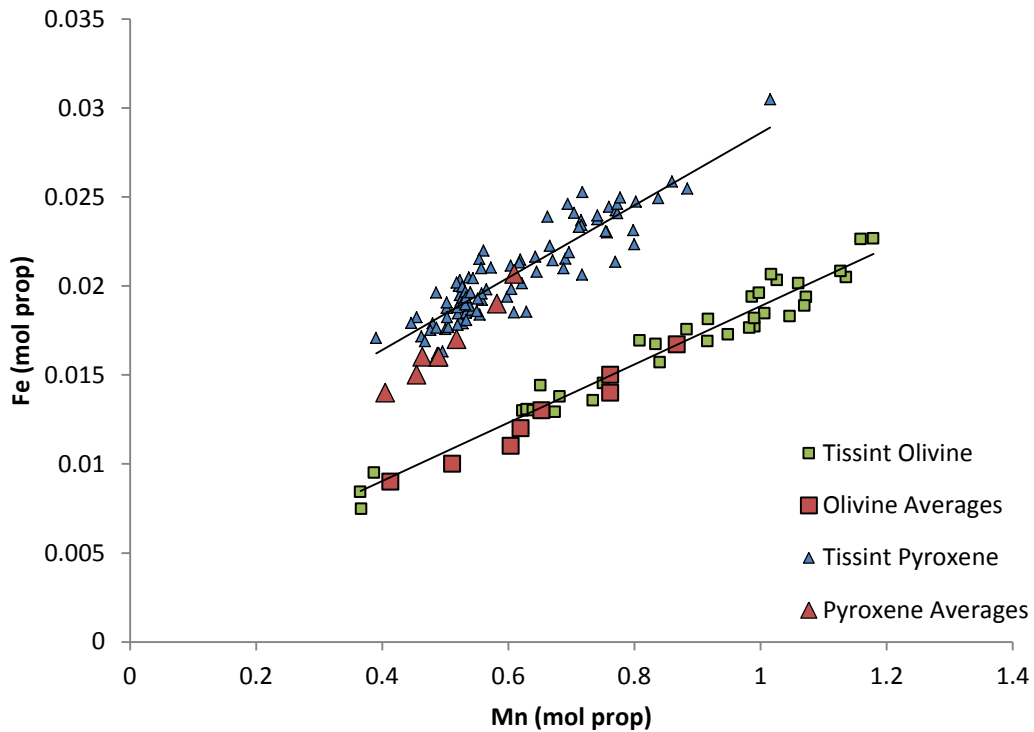


**Fig. 9.** Fe vs. Mn (mol proportion) for olivines and pyroxene. Olivine and pyroxene values measured from this study. Average compositions for other olivine-phyric shergottites from Papike et al. (2009).

### 5.1.2 Olivine

Similar to the pyroxene analyses, there is a positive correlation between Mn and Fe for olivine (Fig. 9). The average Fe/Mn ratio for olivine measured in this study is 50 and is consistent with the value determined by Papike et al. (2003),  $47 \pm 3$ .

Compositions for 37 olivine analyses were calculated and revealed the compositional range to be Fo<sub>39.2</sub>– Fo<sub>81.4</sub> (Fig. 5b). These values are consistent with those measured for olivine cores by Irving and Kuehner (2012). Three olivine core measurements from megacrysts give the most Mg-rich value measured in this study, Fo<sub>81.4</sub>. The Mg# of the melt in equilibrium with this high Mg# would be 0.599, using an olivine-melt Fe-Mg exchange coefficient ( $K_D$ ) value of 0.35 (Filiberto and Dasgupta, 2011). The equation for this exchange coefficient is

$$K_D = (X_{melt}^{Mg} / X_{olivine}^{Mg}) / (X_{melt}^{Fe^{2+}} / X_{olivine}^{Fe^{2+}}) \quad (\text{Equation 4})$$

where X is the mole fraction of the component in the phase. This  $K_D$  value is used to determine if olivine in shergottites were in equilibrium with the melt it crystallized from, and, therefore, could represent a magma composition (Filiberto and Dasgupta, 2011). Fig. 10 is a plot of bulk Mg# against average olivine core Fo content, or Mg#, for Tissint and other shergottites. The curve represents the calculated Mg# of olivine in equilibrium of the melt, using  $K_D$  value of  $0.35 \pm 0.1$  (Filiberto and Dasgupta, 2011). As seen in Fig. 10, there are four olivine-phyric shergottites that fall on or near the equilibrium line; Y-980459, Northwest Africa (NWA) 5789, Tissint, and NWA 2990. Although the bulk and olivine core compositions of Larkman Nunatak (LAR) 06319 do not represent the parent melt, melt inclusions within the olivine indicate a near parental melt composition (Peslier et al., 2010). Since Tissint lies directly on this equilibrium line, the olivine cores were likely in equilibrium with the melt during crystallization.

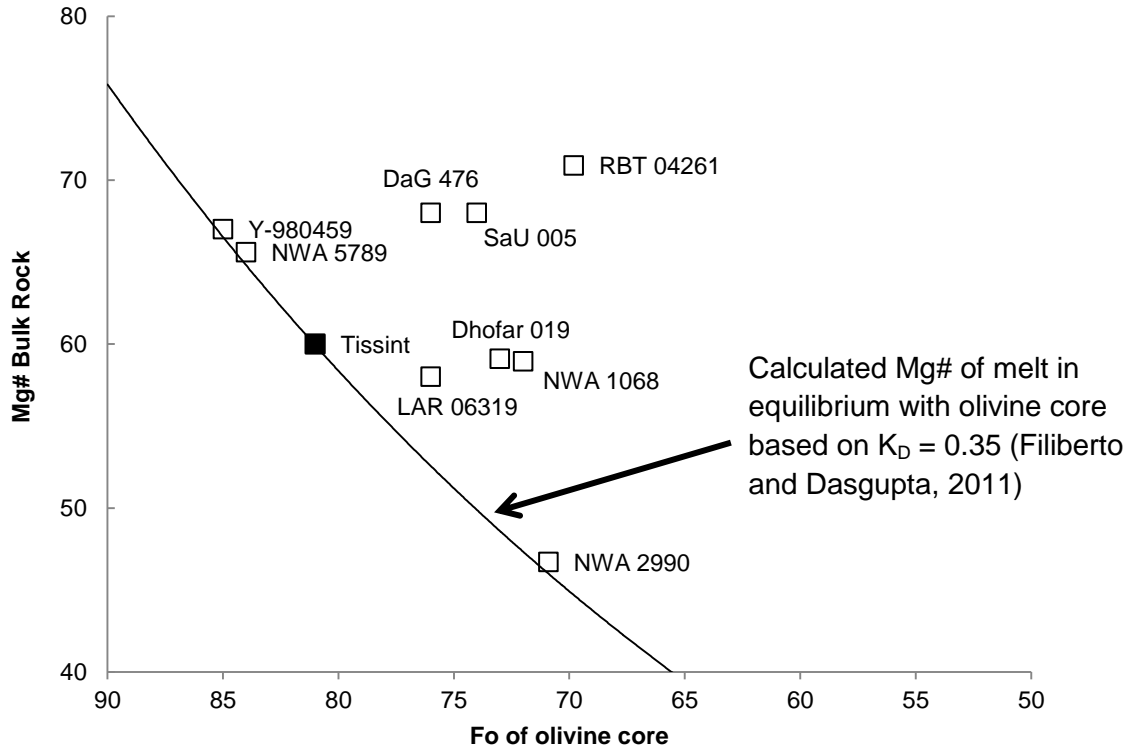


**Fig. 10.** Bulk Mg# plotted against Fo content of olivine macrocryst cores for olivine-phyric shergottites. Black line represents the calculated Mg# of the melt in equilibrium with the olivine core based on  $K_D = 0.35$  from Filiberto and Dasgupta (2011). Data from Zipfel et al. (2000), Mikouchi et al. (2001), Barrat et al. (2002), Taylor et al. (2002), Goodrich et al. (2003), Greshake et al. (2004), Shearer et al. (2008), Usui et al. (2008), Basu Sarbadhikari et al. (2009), Bunch et al. (2009), Peslier et al. (2010), Gross et al. (2011), Chennaoui Aoudjehane et al. (2012), and this study. Abbreviation for meteorite not addressed in the text is Roberts Massif (RBT) 04261. Modified from Filiberto and Dasgupta (2011).

### 5.1.3 Plagioclase

Papike et al. (2003) determined that the plagioclase content in the shergottites is related to its REE enrichment. Fig. 11 shows chondrite normalized La/Yb ratio of the bulk rock of various shergottites plotted against the  $K_2O/Na_2O$  in weight percent of plagioclase multiplied by the by  $Al_2O_3$  weight percent. This plot shows a positive trend from depleted to enriched shergottites with each enrichment classifications (depleted, intermediate, and enriched) plotting as a separate group (Papike et al., 2009). Tissint lies within the depleted shergottites as expected.

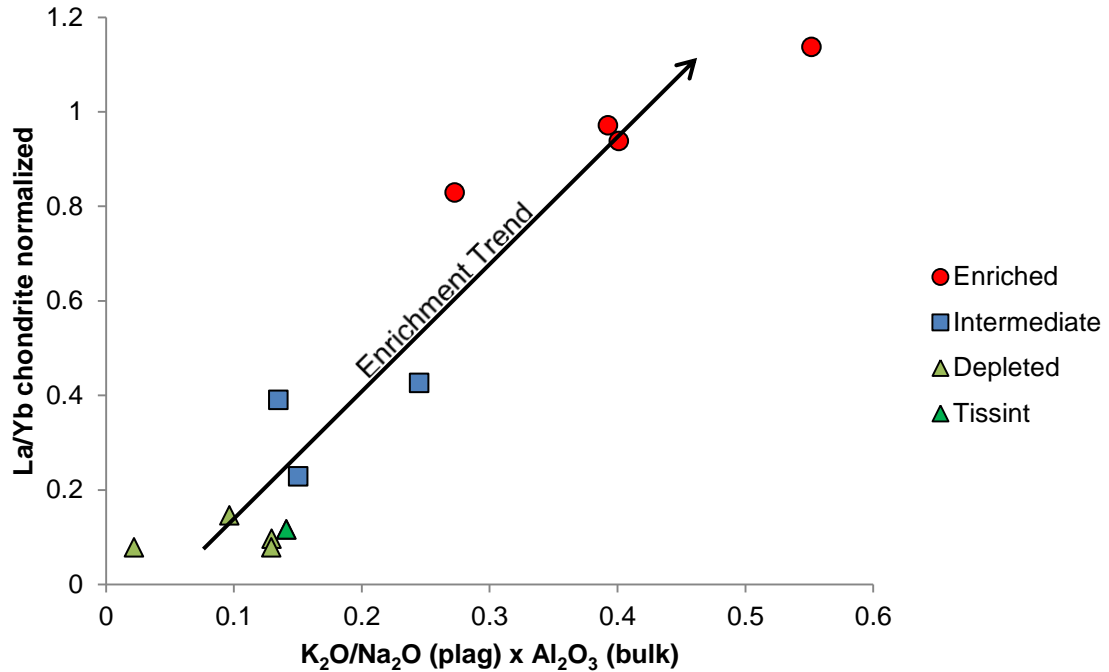


**Fig. 11.** Comparison of La/Yb (bulk rock chondrite normalized) vs  $K_2O/Na_2O$  (plagioclase wt %) x  $Al_2O_3$  (bulk rock wt %) for plagioclase in Tissint and other shergottites. La/Yb normalized to chondrite values of Anders and Grevesse (1989). Data from Dreibus et al. (1982; 1996; 2000), Burghese et al. (1983), Treiman et al. (1994), Warren et al. (1996), Rubin et al. (2000), Zipfel et al. (2000), Barrat et al. (2001; 2002), Anand et al. (2008), Papike et al. (2009), Irving et al. (2010), Gross et al. (2011), Chennaoui Aoudjehane et al. (2012), and this study. Modified from Papike et al. (2009).

#### 5.1.4 Oxides

The redox state of rock, reported as oxygen fugacity ( $f_{O_2}$ ), is useful in determining the physical conditions of the source when crystallization began. The redox state is determined from reduction-oxidation (redox) reactions in which an ion changes oxidation state. For example,  $Fe^{2+}$  changes oxidation state to  $Fe^{3+}$  when oxygen reacts with magnetite to form hematite. Oxygen fugacity can be used as a monitor of the chemical potential, or partial molar Gibbs free energy of oxygen in a system and is measured by the change in free energy between oxidation states in a redox reaction (Frost, 1991; Best, 2003).

In this study, oxygen fugacity and crystallization temperatures are estimated using the olivine-pyroxene-spinel (Ol-Px-Sp) oxybarometer developed by Sack and

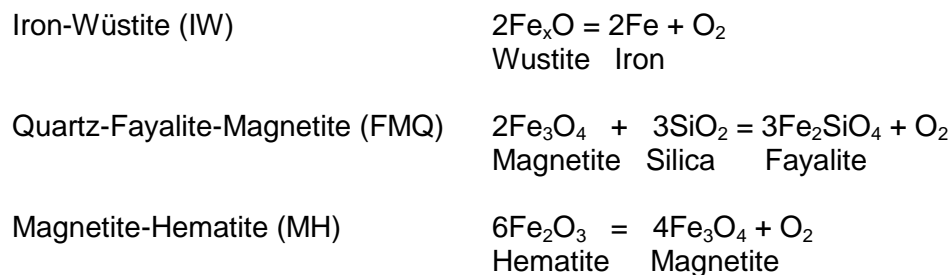
Ghiorso (1989; 1991a; 1991b; 1994a; 1994b; 1994c) and the Fe-Ti oxide geothermobarometer developed by Ghiorso and Evans (2008). Online calculators for these barometers are located on the Computational Thermodynamics (CT) Server ([http://ctserver.ofm-research.org/Olv\\_Spn\\_Opx/index.php](http://ctserver.ofm-research.org/Olv_Spn_Opx/index.php), <http://ctserver.ofm-research.org/OxideGeothrm/OxideGeothrm.php>).

The Ol-Px-Sp oxybarometer utilizes an equilibrium assemblage of olivine, orthopyroxene, and spinel. Based on an olivine-pyroxene Fe-Mg exchange coefficient of  $K_D = 1.2$ , the composition of the first pyroxenes to crystallize in equilibrium with olivine ( $Fo_{69}$ ) is  $Wo_5En_{68}Fs_{27}$  (Longhi and Pan, 1989). To identify the oxides that likely formed in equilibrium with these olivine and pyroxene compositions, the oxides were chosen based on the criteria selected by Goodrich et al. (2003). Their criteria consisted of chromite grains with the highest Cr# (molar Cr/Cr + Al) and lowest Fe# (molar Fe/Fe + Mg) because a chromite with these values indicate the earliest crystallization and the least amount of re-equilibration in the system, respectively. Based on this criteria, three chromite grains were chosen with Cr# = 81-84 and Fe# = 75-86. The results from the oxybarometer calculations at 1 bar are listed Table 5 and the oxide weight percent compositions of the olivine, pyroxene, and chromites used are listed in Appendix 2.

The Fe-Ti geothermobarometer utilizes late-stage oxides magnetite and ilmenite to estimate crystallization temperature and oxygen fugacity. Since magnetite was not analyzed in this sample, titanomagnetite grains with the highest magnetite (10-18 %) and high *ülvospinel* (66-73%) endmember compositions were used in the calculations (Gross et al., 2013). The oxide grains used in these calculations occur separately throughout the groundmass in the sample and not in close proximity to each other. The results of the geothermobarometer calculations from seven titanomagnetite and four

ilmenite grains are listed in Table 5 and the oxide weight percent compositions of the selected grains are listed in Appendix 2.

Oxygen buffers are redox reactions that maintain the equilibrium between pure solids and melt in a system. These buffers are typically used as references for describing the oxygen fugacity of a natural system and may not be present in natural systems (Herd, 2008). Three common oxygen buffers used for oxygen fugacity comparisons are iron-wüstite (IW), quartz-fayalite-magnetite (FMQ), and magnetite-hematite (MH). These reactions are listed below (Frost, 1991).



The oxygen fugacity of these buffers is calculated using a fixed temperature and pressure, namely the values from an oxybarometer. Table 5 lists the buffer values as the log unit differences from the oxygen fugacity calculated using the OI-Px-Sp oxybarometer and Fe-Ti geothermometer. The equations used to calculate the oxygen buffers are listed in Appendix 3.

Temperatures calculated from the OI-Px-Sp oxybarometer range from 845 to 1180°C with an average of  $1044 \pm 352$  °C ( $2\sigma$ ). The average oxygen fugacity values are IW –  $0.17 \pm 1$ , FMQ –  $3.80 \pm 0.9$ , and MH –  $9.03 \pm 0.9$  (log units,  $2\sigma$  standard error). The temperatures and oxygen fugacity values are consistent with previously published data from Castle and Herd (2013) and Herd et al. (2013). Castle and Herd (2013) yielded a temperature range of 950 to 1300 °C and oxygen fugacity values of IW +  $0.36 \pm 0.07$  and FMQ –  $3.24 \pm 0.05$  (log units,  $1\sigma$  standard error). Herd et al. (2013) obtained a temperature range of 1474 to 775°C and average oxygen fugacity values of IW –  $0.1 \pm$

0.5 and FMQ –  $3.8 \pm 0.4$  (log units,  $1\sigma$  standard error). The low oxygen fugacity is similar to other olivine-phyric shergottites Dhofar (Dho) 019, Y-980459, NWA 5789, SaU 005, and Queen Alexandria (QUE) 94201 (Herd et al., 2013).

The Fe-Ti geothermometer calculations yielded a temperature range of 784 – 1184°C with an average temperature of  $1006 \pm 226$  °C based on 28 calculations between seven titanomagnetite grains and four ilmenite grains. This average temperature is more than 200 degrees lower than that of Castle and Herd (2013) at  $1220 \pm 20$  °C ( $1\sigma$ ). The average oxygen fugacity values are IW +  $2.53 \pm 0.8$ , FMQ –  $1.13 \pm 1.1$ , and MH –  $6.71 \pm 1.1$  (log units,  $2\sigma$ ) and are within error of the values of IW +  $2.37 \pm 0.04$  and FMQ –  $1.06 \pm 0.03$  (log units,  $1\sigma$ ) presented by Castle and Herd (2013).

The results from both of these barometers indicate that the Tissint magma became more oxidized between crystallization of early olivine to the late-stage oxides. This is based on the shift from IW – 0.17 to IW + 2.53, from FMQ – 3.8 to FMQ – 1.13, and from MH – 9.03 to MH – 6.71 (Castle and Herd, 2013; Gross et al., 2013). The oxygen fugacity value of FMQ – 3.8 lies near the lower end of the range of oxygen fugacities (FMQ – 4.2 to FMQ -2) thought to represent the redox state of the Martian mantle (Peslier et al., 2010). The change in oxygen fugacity by over 2 log units could be the result of ferric iron buildup as crystallization progresses, similar to that suggested for LAR 06319 and NWA 6234 (Peslier et al., 2010; Gross et al., 2013).

**Table 5.** Oxybarometry results

	T (°C) <sup>a</sup>	log <sub>10</sub> f <sub>O<sub>2</sub></sub>	log <sub>10</sub> f <sub>O<sub>2</sub></sub> (IW) <sup>b</sup>	log <sub>10</sub> f <sub>O<sub>2</sub></sub> (FMQ) <sup>c</sup>	log <sub>10</sub> f <sub>O<sub>2</sub></sub> (MH) <sup>d</sup>
Ol-Px-Sp	1044 ± 352	-14.6 ± 5.8	-0.17 ± 1.0	-3.80 ± 0.9	-9.37 ± 0.9
Fe-Ti	1006 ± 226	-12.4 ± 4.6	2.53 ± 0.8	-1.13 ± 1.1	-6.71 ± 1.1

Errors are 2σ standard deviation.

<sup>a</sup>Temperature calculated from the CT server, Ol-Px-Sp oxybarometer of Ghiorso and Sack (1991) and Fe-Ti geothermometer of Ghiorso and Evans (2008)

<sup>b</sup>Relative to the Iron-Wüstite (IW) buffer as defined by Herd (2008) after O'Neill (1988)

<sup>c</sup>Relative to the Quartz-Fayalite-Magnetite (FMQ) buffer as defined by Herd (2008) after Wones and Gilbert (1969)

<sup>d</sup>Relative to the Magnetite-Hematite (MH) buffer as defined by Herd (2008) after Frost (1991)

## 5.2 Crystallization Ages

The Lu-Hf and Sm-Nd ages of 570 ± 84 Ma and 690 ± 140 Ma, respectively, calculated in this study indicate Tissint is the oldest known shergottite, except possibly for Dhofar 019 with an age of 586 ± 9 Ma (Borg et al., 2001). These ages are consistent and within uncertainty of other ages calculated for Tissint, listed in Table 6, by Brennecka et al. (2012; 2013) and Park et al. (2013). The ranges in ages and precision could be a result of the samples and methods used for each study. Glass pockets and melt inclusions observed in Tissint, particularly in olivine, could affect the isotopic measurements and, subsequently, the age calculations.

Since there is a wide range of ages and precision between those previously published and this study, a weighted average of the internal isochron ages was calculated using the <sup>147</sup>Sm-<sup>143</sup>Nd and <sup>87</sup>Rb-<sup>87</sup>Sr ages of Brennecka et al. (2013), the <sup>87</sup>Rb-<sup>87</sup>Sr age of Park et al. (2013), and both ages from this study. The calculated weighted average age is 597 ± 27 Ma and is shown in Fig. 12. This age is a better representation for Tissint because it is constrained by results from independent isotopic systems into a more precise age.

Fig. 13 shows a comparison of the ages of Tissint (this study) with other shergottites. From Fig. 13, it is apparent that the ages of the shergottites correlate with

their enrichment classification. Tissint has the oldest crystallization age and plots with the group of depleted shergottites, which are significantly older than the enriched and intermediate shergottites.

In Fig. 13, the meteorites with an ejection age similar to Tissint (~1.1 Ma) include DaG 476, Y-980459, and NWA 1195 (Nishiizumi et al., 2012). The rest of the depleted shergottites range between 1.5 – 19.8 Ma indicating the depleted shergottites were ejected from Mars during multiple ejection events and the crystallization ages do not necessarily correlate with ejection ages (Nyquist et al., 2001). For example, Dhofar 019 has a similar crystallization age ( $586 \pm 9$  Ma) to Tissint, however, the ejection ages differ by about 18.7 Ma (Borg et al., 2001; Nyquist et al., 2001). This difference indicates that Tissint and Dhofar 019 sources are likely not related and they both came from different ejection events.

**Table 6.** Ages determined for Tissint from previously published and reported data and this study.

System	Age	Uncertainty ( $2\sigma$ )	Source
$^{147}\text{Sm}-^{143}\text{Nd}$	596	23	Brennecka et al. (2012)
$^{147}\text{Sm}-^{143}\text{Nd}$	590	12	Brennecka et al. (2013)
$^{87}\text{Rb}-^{87}\text{Sr}$	560	30	Brennecka et al. (2013)
$^{87}\text{Rb}-^{87}\text{Sr}$	621	17	Park et al. (2013)
$^{40}\text{Ar}/^{39}\text{Ar}$	610	33	Park et al. (2013)
$^{147}\text{Sm}-^{143}\text{Nd}$	690	140	This Study
$^{176}\text{Lu}-^{176}\text{Hf}$	570	84	This Study

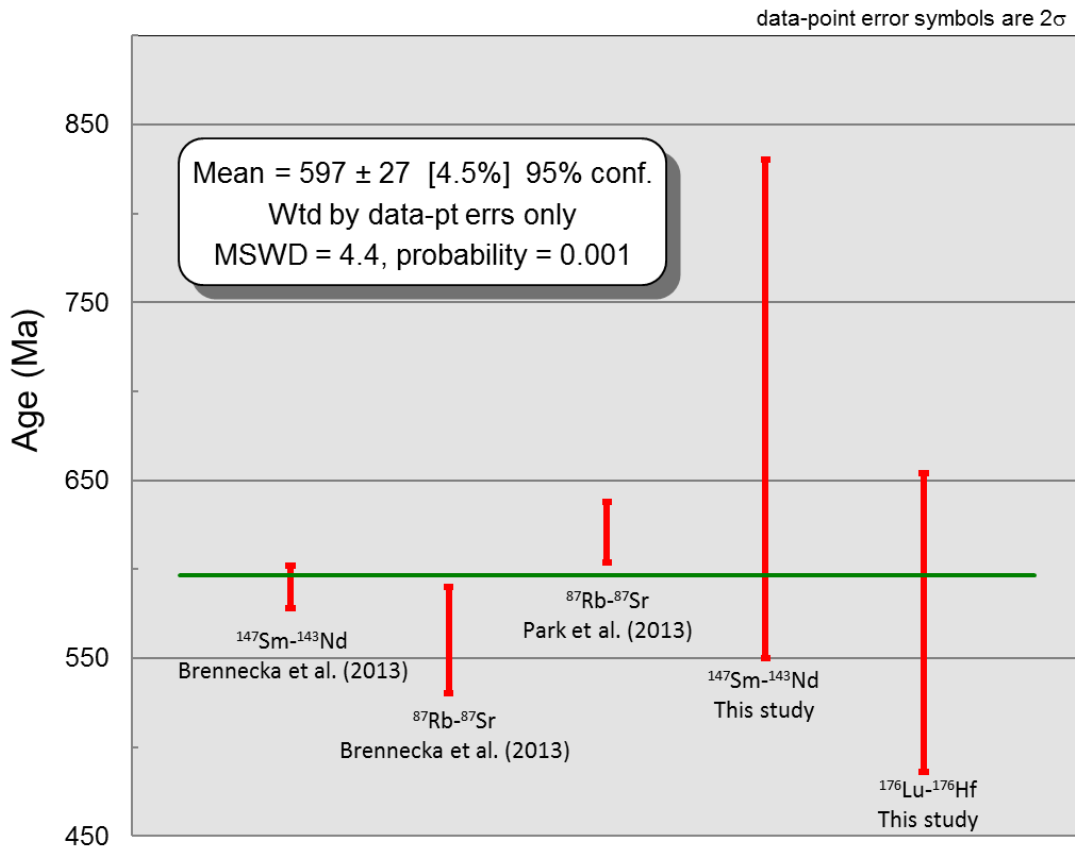


**Figure 12.** Weighted average for all internal isochron ages. Ages listed in Table 6.

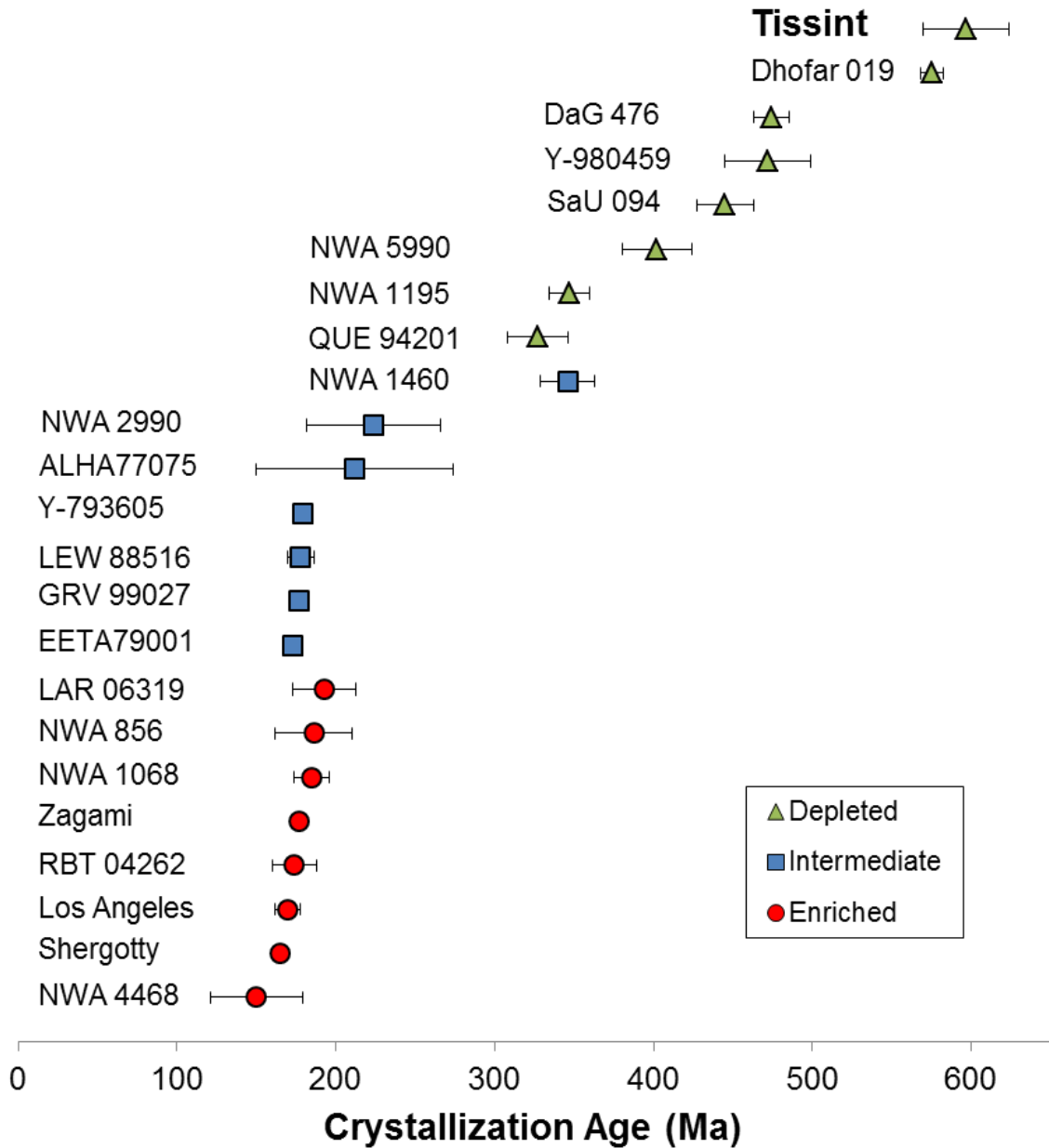


**Figure 13.** Ages for shergottites. Ages from Borg et al. (1997; 2001; 2003; 2008), Misawa et al. (1997), Nyquist et al. (2001; 2009), Shih et al. (2003; 2005; 2007; 2009; 2011), Brandon and Nyquist (2004), Symes et al. (2008), Shafer et al. (2010), Liu et al. (2011), Lapen et al. (2013) and this study. Abbreviations for meteorites not addressed in the text are Lewis Cliff (LEW) 88516, Grove Mountains (GRV) 99027, and Roberts Massif (RBT) 04261.

## 5.3 Source Compositions

### 5.3.1 $\epsilon^{176}\text{Hf}$ and $\epsilon^{143}\text{Nd}$

The initial  $\epsilon^{176}\text{Hf}$  and  $\epsilon^{143}\text{Nd}$  values are useful in understanding the composition of the source. Table 7 lists the preferred ages of multiple shergottites along with their initial  $^{176}\text{Hf}/^{177}\text{Hf}$  and  $^{143}\text{Nd}/^{144}\text{Nd}$  ratios, initial  $\epsilon^{176}\text{Hf}$  and  $\epsilon^{143}\text{Nd}$  values, and calculated source compositions. For Tissint, the initial  $\epsilon^{176}\text{Hf}$  and  $\epsilon^{143}\text{Nd}$  values and source compositions were calculated using the preferred weighted average age of  $596 \pm 27$  Ma and whole rock isotopic compositions.

The calculated initial  $\epsilon^{176}\text{Hf}$  for Tissint is  $+57.8 \pm 0.9$ , nearly 10 epsilon units higher than that of QUE 94201 at +49.5 and DaG 476 at +50.4 (Blichert-Toft et al., 1999; Debaille et al., 2008). The calculated  $\epsilon^{143}\text{Nd}$  value is  $+41.6 \pm 1.5$ , close to values for DaG 476 (+38.9) and SaU 008 (+39.1), and lower than for QUE 94201 (+47.6) (Borg et al., 1997; Debaille et al., 2008). This value is also consistent with that calculated by Brennecka et al. (2012; 2013) of  $+41.9 \pm 0.53$ . The initial  $\epsilon^{176}\text{Hf}$  and  $\epsilon^{143}\text{Nd}$  values indicate Tissint was derived from one of the most depleted Martian mantle sources yet measured.

### 5.3.2 Source Composition

The  $^{176}\text{Lu}/^{177}\text{Hf}$  and  $^{147}\text{Sm}/^{144}\text{Nd}$  source compositions are calculated using Equation 5 following Borg et al. (1997; 2003) and Lapen et al. (2010). The calculations assume a chondritic bulk Mars and a source differentiation age of 4.513 Ga.

$$\text{Source} = \frac{\left(\frac{\text{daughter}}{\text{ratio}}\right)_{\text{sample}}^T - \left(\frac{\text{daughter}}{\text{ratio}}\right)_{\text{CHUR}}^{T_0} - \left[\left(\frac{\text{parent}}{\text{ratio}}\right)_{\text{sample}}^T * e^{\lambda T}\right]}{e^{\lambda T_0} - e^{\lambda T}} \quad (\text{Equation 5})$$

Where  $\lambda$  is the decay constant, T is the crystallization age of the sample, and  $T_0$  is the source differentiation age. The values for the parent and daughter ratios at the time of

crystallization are the calculated initial ratio values from the isochron. Present-day CHUR isotope ratios used in all calculations are  $^{176}\text{Hf}/^{177}\text{Hf} = 0.282785$ ,  $^{176}\text{Lu}/^{177}\text{Lu} = 0.0336$ ,  $^{143}\text{Nd}/^{144}\text{Nd} = 0.512637$ , and  $^{147}\text{Sm}/^{144}\text{Nd} = 0.1964$  (Bouvier et al., 2008a).

The calculated source  $^{176}\text{Lu}/^{177}\text{Hf}$  and  $^{147}\text{Sm}/^{143}\text{Nd}$  ratios for Tissint and other shergottites are listed in Table 7. The calculated source  $^{176}\text{Lu}/^{177}\text{Hf}$  ratio is 0.0548; similar to those for other depleted shergottites DaG 476 (0.0515) and SaU 008 (0.0507) (calculated from Debaille et al., 2008). The calculated source  $^{147}\text{Sm}/^{144}\text{Nd}$  ratio is 0.279, identical to the ratio presented in Brennecka et al. (2012; 2013), and similar to the calculated source compositions for QUE 94201 (0.284), DaG 476 (0.271), and SaU 008 (0.271) (calculated from Borg et al., 1997; Debaille et al., 2008).

In Fig. 14, Tissint's source compositions are plotted on the binary mixing line for the  $^{147}\text{Sm}/^{144}\text{Nd}$  and  $^{176}\text{Lu}/^{177}\text{Hf}$  source ratios defined by enriched, intermediate, and depleted shergottites. The binary mixing line is based on source compositions of residual trapped liquids (enriched end-member) and cumulates (depleted end-member) in the upper mantle assemblage (UM1) of Debaille et al. (2008) produced in a 1350 - 2000 km deep magma ocean. Tissint plots as a depleted end-member and close to the mixing curve. Calculated source compositions indicate Tissint is derived from a source that is the most depleted in trace elements, and has the largest fraction of cumulates to residual trapped liquids compared to other shergottites (Lapen et al., 2010). The location of Tissint on this mixing array improves the definition of the depleted end-member on this mixing curve.

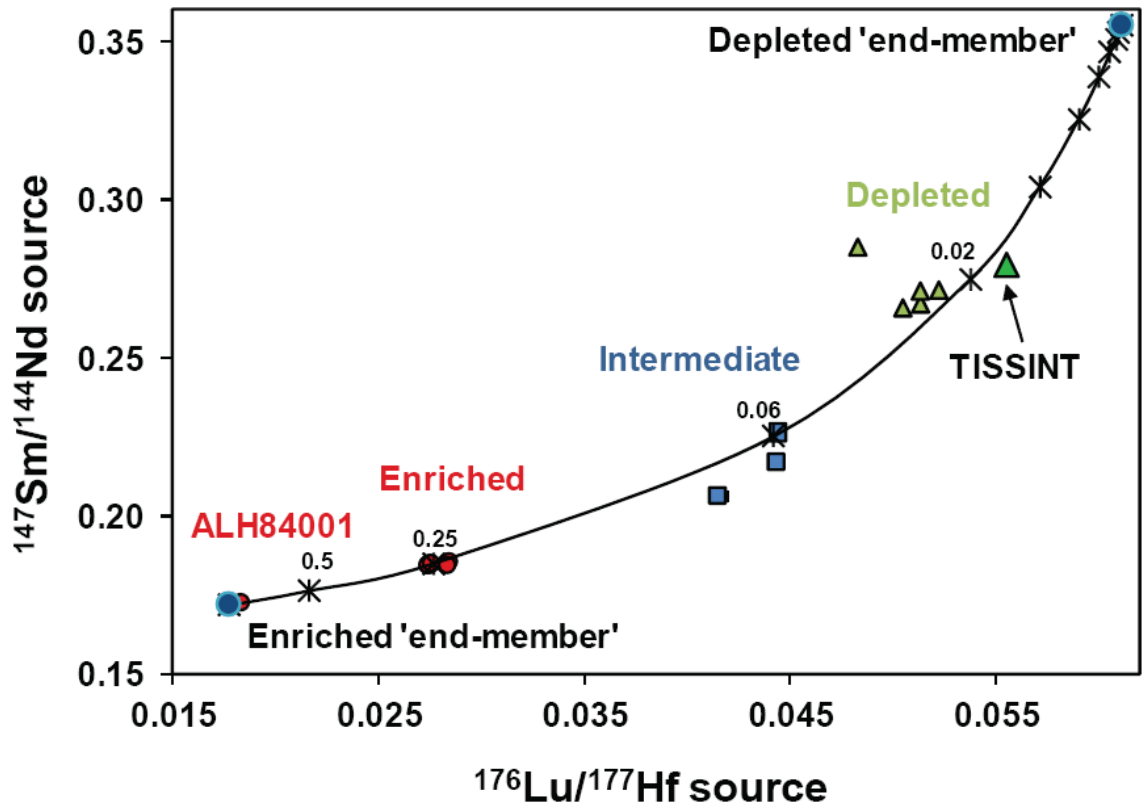


**Fig. 14.** Mixing diagram for shergottites and ALH 84001  $^{147}\text{Sm}/^{144}\text{Nd}$  and  $^{176}\text{Lu}/^{177}\text{Hf}$  source compositions. Red dots are shergottites; DS = depleted shergottites; IS = intermediate shergottites; ES = enriched shergottites; ALH = ALH 84001. The black binary mixing line is based on source compositions of cumulates (depleted end-member) in the upper mantle assemblage (UM1) of Debaille et al. (2008) produced in a 1350 - 2000 km deep magma ocean. Isotope data used for the source calculations of shergottites come from Blichert-Toft et al. (1999), Borg et al. (1997; 2003), Bouvier et al. (2005; 2008b), Debaille et al. (2007; 2008), Lapen et al. (2009; 2010), Shih et al. (2009) and this study. Labeled mixing proportions (black symbols) are based on the fractions of residual trapped liquid (Lapen et al., 2010).

**Table 7.** Ages and Lu-Hf and Sm-Nd isotope data for ALH 84001 and shergottites.

Name	Age (Ma)	$^{176}\text{Hf}/^{177}\text{Hf}_o$	Initial $\epsilon^{176}\text{Hf}$	$^{176}\text{Lu}/^{177}\text{Hf}$ source	$^{143}\text{Nd}/^{144}\text{Nd}_o$	$^{143}\text{Sm}/^{144}\text{Nd}$ source	Initial $\epsilon^{143}\text{Nd}$
NWA 4468	150	0.282166	-17.9	0.0278	0.512091	0.187	-6.8
Shergotty	165	0.282266	-16.9	0.0282	0.512314	0.187	-6.8
Los Angeles	170	0.282334	-13.6	0.0292	0.512335	0.188	-6.3
EETA79001A	173	0.283680	+32.7	0.0447	0.513731	0.229	+17.0
ALH 77005	173	0.283574	+29.7	0.0437	0.512836	0.214	+8.3
RBT 04262	174	0.282135	-18.0	0.0277	0.512071	0.187	-6.6
Zagami	177	0.282248	-16.9	0.0281	0.512314	0.187	-6.8
LAR 06319	183	0.282141	-18.4	0.0276	0.512033	0.186	-7.1
NWA 856	186	0.282285	-15.6	0.0286	0.512319	0.187	-6.7
QUE 94201	327	0.283897	+42.5	0.0483	0.514655	0.287	+47.7
SaU 094	446	0.284120	+45.8	0.0499	0.515270	0.268	+36.3
DaG 476	474	0.284277	+50.0	0.0515	0.515548	0.274	+39.0
Tissint	597	0.284060	+57.8	0.0548	0.513760	0.279	+41.6
ALH 84001	4091	0.284116	-4.0	0.0223	0.512266	0.197	-1.7

Note: Ages and isotope data from Borg et al. (1997; 1998; 2001; 2008), Blichert-Toft et al. (1999), Debaille et al. (2008), Shih et al. (2009), Lapen et al. (2008; 2009; 2010), Shafer et al. (2010), and this study.

## 5.4 Martian Mantle Sources

The binary mixing line defined by shergottite source compositions (Fig. 14) appears to show clustering of the enriched, intermediate, and depleted groups of shergottites. Each group forms its own cluster and lies in a unique position on the array without overlap to another group. Whether these come from distinct sources or are 'snapshots' of a continuum of mixing proportions is an unanswered question. In general, the source compositions of these groups show a correlation with crystallization age. The oldest shergottites plot near the depleted end-member whereas the youngest shergottites lie near the enriched end-member.

The  $^{176}\text{Lu}/^{177}\text{Hf}$  and  $^{147}\text{Sm}/^{144}\text{Nd}$  source compositions of 0.0548 and 0.279, respectively, establish Tissint as the most depleted shergottite. Based on the binary mixing model, Tissint has incorporated the least amount of the enriched component and is the shergottite that is closest in composition to mafic cumulates (Lapen et al., 2010). Initial depletion of mantle sources was the result of crystallization of a magma ocean (Borg et al., 1997). During cooling of the magma ocean, cumulate fractions separate from the magma and sink to the bottom of the magma ocean forming the depleted end-member. Quenched late-stage residual trapped liquids form the enriched end-member and remain near the top of the crystallized magma ocean (Debaille et al., 2008). These two reservoirs are later partially melted through adiabatic decompression in a convective mantle upwelling resulting in volcanism and crystallization of shergottites (Kiefer, 2003; Debaille et al., 2008). The convection of the Martian mantle must have remained stable and inefficient in homogenization for most of the planet's history to maintain isotopic heterogeneity (Kiefer, 2003; Debaille et al., 2008).

Multiple partial melting events before separation from the source could be the cause of variations in trace element and isotopic compositions observed among the

shergottites. Modeling for partial melting events and source compositions determined that the source for QUE 94201 underwent four distinct events around 327 Ma (Borg et al., 1997). Since Tissint shows a similar REE pattern to QUE 94201 (Fig. 6) and derived from a source that is the most depleted in Lu/Hf, Tissint may have experienced similar partial melting events as QUE 94201.

Although Tissint supports the binary mixing model and improves the definition of the depleted end-member, the question of why QUE 94201 plots so far from the line is raised. A third component or phase in the Martian mantle source was suggested by Borg et al. (2003) to account for EETA 79001 plotting off the  $^{147}\text{Sm}/^{144}\text{Nd}$  source versus  $^{87}\text{Rb}/^{86}\text{Sr}$  source. An additional component or phase may explain why QUE 94201 plots far from the line, but additional examination or re-analyzing of isotopic compositions may be needed to determine the accuracy of QUE 94201's position on the  $^{147}\text{Sm}/^{144}\text{Nd}$  source vs  $^{176}\text{Lu}/^{177}\text{Hf}$  source mixing model.

Modeling of meteorite and mantle cumulate source compositions has revealed possible mantle mineralogical compositions. Borg et al. (2003) modeled meteorite and magma ocean cumulate source compositions using bulk cumulate compositions (ol:opx:cpx:grt = 50.2:30.5:18.3:0.7 and ol:opx:cpx:grt:amph = 49.8:30.41:18.3:0.7:0.8) to calculate source compositions for multiple stages of crystallization. This model showed little variation in  $^{176}\text{Lu}/^{177}\text{Hf}$  and  $^{147}\text{Sm}/^{144}\text{Nd}$  source compositions with amphibole present in the source, which primarily affects the Rb and Sr compositions. The  $^{176}\text{Lu}/^{177}\text{Hf}$  source compositions calculated for bulk cumulates with and without amphibole were 0.046 and 0.048, respectively, and were consistent with the calculated source composition for QUE 94201. However, Tissint's  $^{176}\text{Lu}/^{177}\text{Hf}$  source composition of 0.0548 indicates that the bulk cumulate source composition is actually more depleted in Hf than this model suggests. Based on a two-stage partial melting model by Debaille

et al. (2008), a mineralogical composition of 60% olivine, 9% orthopyroxene, 21% clinopyroxene, and 10% garnet for the upper Martian mantle, where the shergottites are thought to derive. Garnet is the key component in mantle source mineralogy that affects Lu/Hf and Sm/Nd ratios because it is able to strongly fractionate the Lu/Hf ratio and not the Sm/Nd ratio of the modeled melts (Borg et al., 2003). Since these models were limited to a few depleted shergottites, Tissint's highly depleted composition could provide new insights into the possible mineralogy of mantle sources.

The  $^{176}\text{Lu}/^{177}\text{Hf}$  source composition of Tissint extends the upper limit for the range of  $^{176}\text{Lu}/^{177}\text{Hf}$  source compositions for depleted shergottites to 0.0548 from 0.0499 (Debaille et al., 2008). The extension in compositional range helps to fill in the gap between the source compositions of the groups and end-members. The recent arrival of Tissint to Earth offers the possibility that samples with the "missing" compositions may have yet to arrive to Earth. Also, all Martian meteorite samples that have been recovered have not undergone the same amount of research as those mentioned in this study. It is also possible that the samples that could fill the gaps have been recovered but not studied for isotope composition and source compositions. If sample bias is the cause for the grouping observed in the binary mixing array, then it is plausible that the "missing" compositions have yet to be measured or found. Analyses of samples like Tissint give us more insight into Mars' composition, history, and geological process. Understanding the history and processes of Mars helps us to understand those of other planetary bodies, such as Earth.

## Chapter 6

### Conclusion

Elemental and mineralogical analyses of Tissint confirm its classification as a depleted olivine shergottite. The macrocryst olivine core compositions with  $Fo_{69}$  are in equilibrium with the bulk rock Mg# of 59.9 using an olivine-melt  $K_D = 0.35$  (Filiberto and Dasgupta, 2010). Pyroxene compositions show a crystallization trend from orthopyroxene and pigeonite to augite, similar to other olivine-phyric shergottites. Calculations using an olivine-pyroxene-spinel oxybarometer and Fe-Ti geothermobarometer reveal oxidation of Tissint between crystallization of equilibrium oxides and silicates to late-stage oxides.

Isotopic analyses of Tissint yield  $^{176}\text{Lu}$ - $^{176}\text{Hf}$  and  $^{147}\text{Sm}$ - $^{143}\text{Nd}$  isochron ages of  $570 \pm 84$  Ma and  $690 \pm 140$  Ma, respectively. These ages are consistent with previously published ages by Brennecka et al. (2012, 2013) and Park et al. (2013). A weighted average age of  $597 \pm 27$  Ma was calculated from all internal isochron ages for Tissint. These ages establish Tissint as one of the two oldest shergottites, along with Dhofar 019 which is  $586 \pm 9$  Ma (Borg et al., 2001). Initial daughter ratios of  $^{176}\text{Hf}/^{177}\text{Hf} = 0.284060 \pm 0.000046$  and  $^{143}\text{Nd}/^{144}\text{Nd} = 0.51376 \pm 0.00034$  along with initial  $\epsilon^{176}\text{Hf} (+57.8 \pm 0.9)$  and  $\epsilon^{143}\text{Nd} (+41.6 \pm 1.5)$  values indicate Tissint derived from a depleted magma source.

Tissint's calculated  $^{176}\text{Lu}/^{177}\text{Hf}$  and  $^{147}\text{Sm}/^{144}\text{Nd}$  source ratios of 0.0548 and 0.279, respectively, indicate that Tissint derived from a source that is the most depleted in incompatible trace elements, and has the largest fraction of cumulates to residual rapped liquids (Lapen et al., 2010) compared to other shergottites. The location of Tissint on the binary mixing array defined by enriched, intermediate, and depleted shergottites improves the definition of the depleted end-member on this mixing curve.

## References

- Anand M., James S., Greenwood R. C., Johnson D., Franchi I. A., and Grady M. M. 2008. Mineralogy and geochemistry of shergottites RBT 04262 (abstract#2173). 39th Lunar and Planetary Science Conference. CD-ROM.
- Anders E. and Grevesse N. 1989. Abundances of the elements: Meteoritic and solar. *Geochimica et Cosmochimica Acta* 53:197-214.
- Barrat J., Blichert-Toft J., Nesbitt R. W., Keller F. 2001. Bulk chemistry of Saharan shergottite Dar al Gani 476. *Meteoritics & Planetary Science* 36:23-29.
- Barrat J. A., Jambon A., Bohn M., Gillet Ph., Sautter V., Göpel C., Lesourd M., and Keller F. 2002. Petrology and chemistry of the picritic shergottites North West Africa 1068 (NWA 1068). *Geochimica et Cosmochimica Acta* 66:3505-3518.
- Basu Sarbadhikari A., Day J. M. D., Liu Y., Rumble, III D., and Taylor L. A. 2009. Petrogenesis of olivine-phyric shergottite Larkman Nunatak 06319: Implications for enriched components in Martian basalts. *Geochimica et Cosmochimica Acta* 73:2190-2214.
- Best M. G. 2003. Igneous and metamorphic petrology, 2nd ed. Malden: Blackwell. 729 p.
- Blichert-Toft J., Gleason J. D., Télouk P., and Albarède F. 1999. The Lu-Hf isotope geochemistry of shergottites and the evolution of the Martian mantle-crust system. *Earth and Planetary Science Letters* 173:25-39.
- Bogard D. D. and Johnson P. 1983. Martian Gases in an Antarctic Meteorite? *Science* 221:651-654.
- Borg L. E., Nyquist L. E., Taylor L. A., Wiesmann H., and Shih C.-Y. 1997. Constraints on Martian differentiation processes from Rb-Sr and Sm-Nd isotopic analyses of the basaltic shergottite QUE 94201. *Geochimica et Cosmochimica Acta* 61:4915-4931.
- Borg L. E., Nyquist L. E., Wiesmann H., and Reese Y. 1998. Samarium-Neodymium isotopic systematics of the Iherzolitic shergottite Lewis Cliff 88516. *Meteoritics & Planetary Science* 33:A20.
- Borg L. E., Nyquist L. E., Reese Y., Wiesmann H., Shih C.-Y., Taylor L. A., and Ivanova M. 2001. The age of Dhofar 019 and its relationship to the other Martian meteorites (abstract#1144). 32nd Lunar and Planetary Science Conference. CD-ROM.

- Borg L. E., Nyquist L. E., Reese Y., and Wiesmann H. 2002. Constraints on the petrogenesis of Martian meteorites from the partially disturbed Rb-Sr and Sm-Nd isotopic systematics of LEW88516 and ALH77005. *Geochimica et Cosmochimica Acta* 66:2037-2053.
- Borg L. E., Nyquist L. E., Wiesmann H., Shih C.-Y., and Reese Y. 2003. The age of Dar al Gani 476 and the differentiation history of the Martian meteorites inferred from their radiogenic isotopic systematics. *Geochimica et Cosmochimica Acta* 67:3519-3536.
- Borg L. E., Gaffney A. M., and DePaolo D. 2008. Preliminary age of Martian meteorite Northwest Africa 4468 and its relationship to the other incompatible-element-enriched shergottites (abstract#1851). 39th Lunar and Planetary Science Conference. CD-ROM.
- Bouvier A., Blichert-Toft J., Vervoort J. D., and Albarède F. 2005. The age of SNC meteorites and the antiquity of the Martian surface. *Earth and Planetary Science Letters* 240:221-233.
- Bouvier A., Vervoort J. D., and Patchett P. J. 2008a. The Lu-Hf and Sm-Nd isotopic composition of CHUR: Constraints from unequilibrated chondrites and implications for the bulk composition of terrestrial planets. *Earth and Planetary Science Letters* 273:48-57.
- Bouvier A., Blichert-Toft J., Vervoort J. D., Gillet P. G., and Albarède F. 2008b. The case for old basaltic shergottites. *Earth and Planetary Science Letters* 266:105-124.
- Brandon A. D. and Nyquist L. E. 2004. Rb-Sr and Sm-Nd isotope systematics of shergottite NWA 856: Crystallization age and implications for alteration of hot desert SNC meteorites (abstract#1931). 35th Lunar and Planetary Science Conference. CD-ROM.
- Brennecka G. A., Borg L. E., and Wadhwa M. 2012. The age of Tissint: Sm-Nd & Rb-Sr isotope systematics (abstract). *Meteoritics & Planetary Science* 47 (Suppl.):5157.pdf.
- Brennecka G. A., Borg L. E., Symes S. J. K., and Wadhwa M. 2013. The age of Tissint: Sm-Nd & Rb-Sr isotope systematic of a Martian meteorite fall (abstract#1786). Proceedings, 44th Lunar and Planetary Science Conference. CD-ROM.

- Bunch T. E., Irving A. J., Wittke J. H., Rumble, III D., Korotev R. L., Gellissen M., and Palme H. 2009. Petrology and composition of Northwest Africa 2990: A new type of fine-grained, enriched, olivine-phyric shergottite (abstract#2274). 40th Lunar and Planetary Science Conference. CD-ROM.
- Burghelle A., Dreibus G., Palme H., Rammensee W., Spettel B., Weckwerth G., and Wänke H. 1983. Chemistry of shergottites and the Shergotty parent body (SPB): Further evidence for the two component model of planet formation. 14th Lunar and Planetary Conference, pp. 80-81.
- Castle N. and Herd C. D. K. 2013. Igneous evolution of the Tissint meteorite: Oxide compositions and oxy-thermobarometry (abstract). *Meteoritics & Planetary Science* 48 (Suppl.):5338.pdf.
- Chennaoui Aoudjehane H., Avice G., Barrat J.-A., Boudouma O., Chen G., Duke M. J. M., Franchi I. A., Gattaceca J., Grady M. M., Greenwood R. C., Herd C. D. K., Hewins R., Jambon A., Marty B., Rochette P., Smith C. L., Sautter V., Verchovsky A., Weber P., and Zanda B. 2012. Tissint Martian meteorite: A fresh look at the interior, surface, and atmosphere of Mars. *Science* 338:785-788.
- Debaille V., Brandon A. D., Yin Q.-Z., and Jacobsen B. 2007. Coupled  $^{142}\text{Nd}$ - $^{143}\text{Nd}$  evidence for a protracted magma ocean in Mars. *Nature* 450:252-258.
- Debaille V., Yin Q.-Z., Brandon A. D., and Jacobsen B. 2008. Martian mantle mineralogy investigated by the  $^{176}\text{Lu}$ - $^{176}\text{Hf}$  and  $^{147}\text{Sm}$ - $^{143}\text{Nd}$  systematics of shergottites. *Earth and Planetary Science Letters* 269:186-199.
- Deer W. A., Howie R. A., and Zussman J. 1992. An introduction to the rock-forming minerals, 2nd ed. Harlow: Pearson. 696 p.
- Dreibus G., Palme H., Rammensee W., Spettel B., Weckwerth G., and Wänke H. 1982. Composition of Shergotty parent body; Further evidence of a two component model of planet formation. 13th Lunar and Planetary Science Conference, pp.180-181.
- Dreibus G., Spettel B., Wlotzka F., Schultz L., Weber H. W., Jochum K. P., and Wänke H. 1996. QUE 94201: An unusual Martian basalt. *Meteoritics & Planetary Science* 31:A39.
- Dreibus G., Spettel B., Haubold R., Jochum K. P., Palme H., Wolf D., and Zipfel J. 2000. Chemistry of a new shergottite: Sayh Al Uhaymir 005 (abstract). *Meteoritics & Planetary Science* 35 (Suppl.):5024.pdf.

- Droop G. T. R. 1987. A general equation for estimating Fe<sup>3+</sup> concentrations in ferromagnesian silicates and oxides from microprobe analyses, using stoichiometric criteria. *Mineralogical Magazine* 51:431-435.
- Faure G. and Mensing T. M. 2005. *Isotopes: Principles and applications*. Hoboken: John Wiley & Sons, Inc. 897 p.
- Filiberto J. and Dasgupta R. 2011. Fe<sup>2+</sup>-Mg partitioning between olivine and basaltic melts: Applications to genesis of olivine-phyric shergottites and conditions of melting in the Martian interior. *Earth and Planetary Science Letters* 304:527-537.
- Frost B. R. 1991 Introduction to oxygen fugacity and its petrologic significance. *Reviews in Mineralogy* 25:1-9.
- Ghiorso M. S. and Evans B. W. 2008. Thermodynamics of rhombohedral oxide solid solutions and a revision of the Fe-Ti two-oxide geothermometer and oxygen-barometer. *American Journal of Science* 308:957-1039.
- Goodrich C. A. 2003. Petrogenesis of olivine-phyric shergottites Sayh al Uhaymir 005 and Elephant Moraine A79001 lithology A. *Geochimica et Cosmochimica Acta* 67:3735-3771.
- Goodrich C. A., Herd C. D. K., and Taylor L. A. 2003. Spinels and oxygen fugacity in olivine-phyric and lherzolitic shergottites. *Meteoritics & Planetary Science* 38:1773-1792.
- Greshake A., Fritz J., and Stöffler D. 2004. Petrology and shock metamorphism of the olivine-phyric shergottite Yamato 980459: Evidence for a two-stage cooling and a single-stage ejection history. *Geochimica et Cosmochimica Acta* 68:2359-2377.
- Gross J., Treiman A. H., Filiberto J., and Herd C. D. K. 2011. Primitive olivine-phyric shergottite NWA 5789: Petrography, mineral chemistry and cooling history imply a magma similar to Yamato-980459. *Meteoritics & Planetary Science* 46:116-133.
- Gross J., Filiberto J., Herd C. D. K., Melwani Daswani M., Schwenzer S. P., and Treiman A. H. 2013. Petrography, mineral chemistry, and crystallization history of olivine-phyric shergottite NWA 6234: A new melt composition. *Meteoritics & Planetary Science* 48:854-871.
- Herd C. D. K. 2008. Basalts as probes of planetary interior redox state. *Reviews in Mineralogy & Geochemistry* 68:527-553.

- Herd C. D. K., Duke M. J. M., Bryden C. D., and Pearson D. G. 2013. Tissint among the shergottites: Parental melt composition, redox state, La/Yb and V/Sc (abstract#2683). 44th Lunar and Planetary Science Conference. CD-ROM.
- Irving A. J., Kuehner S. M., Herd C. D. K., Gellissen M., Korotev R. L., Puchtel I., Walker R. J., Lapen T. J., and Rumble, III D. 2010. Petrologic, elemental and multi-isotopic characterization of permafic olivine-phyric shergottite Northwest Africa 5789: A primitive magma derived from depleted Martian mantle (abstract#1547). 41st Lunar and Planetary Science Conference. CD-ROM.
- Irving A. J. and Kuehner S. M. 2012. Extensive magmatic zonation in the mafic silicate phases in Tissint and an evaluation of its excess cumulus olivine content (abstract). *Meteoritics & Planetary Science* 47 (Suppl.):5244.pdf.
- Irving A. J., Kuehner S. M., Tanaka R., Herd C. D. K., Chen G., Lapen T. J. 2012. The Tissint depleted permafic olivine-phyric shergottite: Petrologic, elemental and isotopic characterization of a recent Martian fall in Morocco (abstract#2510). 43rd Lunar and Planetary Science Conference. CD-ROM.
- Kiefer W. A. 2003 Melting in the Martian mantle: Shergottite formation and implications for present-day mantle convection on Mars. *Meteoritics & Planetary Science* 39:1815-1832.
- Lapen T. J., Mahlen N. J., Johnson C. M., and Beard B. L. 2004. High precision Lu and Hf isotope analyses of both spiked and unspiked samples: A new approach. *Geochemistry Geophysics Geosystems* 5:Q01010, doi:10.1029/2003GC000582.
- Lapen T. J., Brandon A. D., Beard B. L., Peslier A. H., Lee C.-T. A., and Dalton H. A. 2008. Lu-Hf age and isotope systematics of the olivine-phyric shergottite RBT 04262 and implications for the sources of enriched shergottites (abstract#2073). 39th Lunar and Planetary Science Conference. CD-ROM.
- Lapen T. J., Righter M., Brandon A. D., Beard B. L., Shafer J., and Irving A. J. 2009. Lu-Hf isotope systematics of NWA 4468 and NWA 2990: Implications for the sources of shergottites (abstract#2376). 40th Lunar and Planetary Science Conference. CD-ROM.
- Lapen T. J., Righter M., Brandon A. D., Debaille V., Beard B. L., Shafer J. T., and Peslier A. H. 2010. A younger age for ALH 84001 and its geochemical link to shergottite sources in Mars. *Science* 328:347-351.

- Lapen T. J., Andreasen, R., Righter M., and Irving A. J. 2013. Lu-Hf age and isotope systematics of intermediate permafic olivine-phyric shergottite NWA 2990: Implications for the diversity of shergottite sources (abstract#2686). 44th Lunar and Planetary Science Conference. CD-ROM
- Lin Y. T., Hu S., Feng L., Zhang J. C., Hao J. L., and Xu L. 2012. Petrography and shock metamorphism of the Tissint olivine-phyric shergottite (abstract). *Meteoritics & Planetary Science* 47 (Suppl.):5131.pdf.
- Liu T., Li C., and Lin Y. 2011 Rb-Sr and Sm-Nd isotopic systematics of the Iherzolitic shergottite GRV 99027. *Meteoritics & Planetary Science* 46:681-689.
- Longhi J. and Pan V. 1989. The parent magmas of the SNC meteorites. 19th Lunar and Planetary Science Conference, pp.451-464.
- McSween, Jr. H. Y. and Treiman A. H. 1998. Martian meteorites. In *Planetary Materials*, edited by Papike J. J. Washington, D.C.: Mineralogical Society of America. pp. 6-1-53.
- Mikouchi T., Miyamoto M., and McKay G. A. 2001. Mineralogy and petrology of the Dar al Gani 476 Martian meteorite: Implications for its cooling history and relationship to other shergottites. *Meteoritics & Planetary Science* 36:531-548.
- Misawa K., Nakamura N., Premo W., and Tatsumoto M. 1997. U-Th-Pb isotopic systematics of Iherzolitic shergottite Yamato-793605. *Antarctic Meteorite Research* 10:95-108.
- Mustard J. F., Herd C. D. K., Skok J. R., and Cannon K. M. 2013. Visible-infrared reflectance of the Tissint meteorite: Impact melt, maskelynite, and implications for Mars remote sensing (abstract#2771). 44th Lunar and Planetary Science Conference. CD-ROM.
- Nishiizumi K., Caffee M. W., and Irving A. J. 2012. Exposure history of Tissint: Evidence for 1.1 million year launch pairing with other depleted olivine-phyric shergottites (abstract). *Meteoritics & Planetary Science* 47 (Suppl.):5349.pdf.
- Nyquist L. E., Wooden J., Bansal B., Wiesmann H., McKay G. A., and Bogard D. D. 1979. Rb-Sr age of Shergotty achondrite and implications for metamorphic resetting of isochron ages. *Geochimica et Cosmochimica Acta* 43:1057-1074.
- Nyquist L. E., Bansal B. M., Wiesmann H., and Shih C.-Y. 1995. "Martians" young and old: Zagami and ALH84001 (abstract#1065). 25th Lunar and Planetary Science Conference. CD-ROM.

- Nyquist L. E., Reese Y. D., Wiesmann H., and Shih C.-Y. 2000. Rubidium-strontium age of Los Angeles shergottite (abstract). *Meteoritics & Planetary Science* 35 (Suppl.):5229.pdf.
- Nyquist L. E., Bogard D. D., Shih C.-Y., Greshake A., Stöfler D., and Eugster O. 2001. Ages and geologic histories of Martian meteorites. *Chronology and Evolution of Mars* 96:105-165.
- Nyquist L. E., Bogard D. D., Shih C.-Y., Park J., Reese Y. D., and Irving A. J. 2009. Concordant Rb-Sr, Sm-Nd, and Ar-Ar ages for Northwest Africa 1460: A 346 Ma old basaltic shergottite related to "Iherzolic" shergottites. *Geochimica et Cosmochimica Acta* 73:4288-4309.
- O'Neill H. S. and Pwenceby M. I. 1993. Thermodynamic data from redox reactions at high temperatures 1. An experimental and theoretical assessment of the electrochemical method using stabilized zirconia electrolytes, with revised values for the Fe-FeO, Co-CoO, N-NiO and Cu-Cu<sub>2</sub>O oxygen buffers, and new data for the W-WO<sub>2</sub> buffer. *Contributions to Mineralogy and Petrology* 114:296-314.
- Papike J. J., Karner J. M., and Shearer C. K. 2003. Determination of planetary basalt parentage: A simple technique using the electron microprobe (abstract#1018). 34th Lunar and Planetary Science Conference. CD-ROM.
- Papike J. J., Karner J. M., Shearer C. K., and Burger P. V. 2009. Silicate mineralogy of Martian meteorites. *Geochimica et Cosmochimica Acta* 73:7443-7485.
- Park J., Herzog G. F., Nyquist L. E., Shih C.-Y., Turrin B., Lindsay F. N., Delaney J. S., Swisher, III C. C., and Agee C. 2013. Ar-Ar and Rb-Sr ages of the Tissint olivine-phyric Martian shergottite (abstract). *Meteoritics & Planetary Science* 48 (Suppl.):5320.pdf.
- Peslier A. H., Hnatyshin D., Herd C. D. K., Walton E. L., Brandon A. D., Lapen T. J., and Shafer J. T. 2010. Crystallization, melt inclusion, and redox history of a Martian meteorite: Olivine-phyric shergottite Larkman Nunatak 06319. *Geochimica et Cosmochimica Acta* 74:4543-4576.
- Rubin A. E., Warren P. H., Greenwood J. P., Verish R. S., Leshin L. A., Hervig R. L., Clayton R. N., and Mayeda T. K. 2000. Los Angeles: The most differentiated basaltic Martian meteorite. *Geology* 28:1011-1014.

- Sack R. O. and Ghiorso M. S. 1989. Importance of considerations of mixing properties in establishing an internally consistent Thermodynamic database - Thermochemistry of minerals in the system  $Mg_2SiO_4$ - $Fe_2SiO_4$ - $SiO_2$ . *Contributions to Mineralogy and Petrology* 102:41-68.
- Sack R. O. and Ghiorso M. S. 1991a. Chromian spinels as petrogenetic indicators: Thermodynamic and petrologic applications. *American Mineralogist* 76:827-847.
- Sack R. O. and Ghiorso M. S. 1991b. An internally consistent model for the thermodynamic properties of Fe-Mg-titanomagnetite-aluminate spinels. *Contributions to Mineralogy and Petrology* 106:474-505.
- Sack R. O. and Ghiorso M. S. 1994a. Thermodynamics of multicomponent pyroxenes. 1. Formulation of a general-model. *Contributions to Mineralogy and Petrology* 116:277-286.
- Sack R. O. and Ghiorso M. S. 1994b. Thermodynamics of multicomponent pyroxenes. 2. Phase-relations in the quadrilateral. *Contributions to Mineralogy and Petrology* 116:287-300.
- Sack R. O. and Ghiorso M. S. 1994c. Thermodynamics of multicomponent pyroxenes. 3. Calibration of  $Fe^{2+}(Mg)_{-1}$ ,  $TiAl_2(MgSi_2)_{-1}$ ,  $TiFe_2^{3+}(MgSi_2)_{-1}$ ,  $AlFe^{3+}(MgSi)_{-1}$ ,  $NaAl(CaMg)_{-1}$ ,  $Al_2(MgSi)_{-1}$  and  $Ca(Mg)_{-1}$  exchange reactions between pyroxenes and silicate melts. *Contributions to Mineralogy and Petrology* 118:271-296.
- Scherer E., Münker C., and Mezger K. 2001. Calibration of the Lutetium-Hafnium clock. *Science* 293:683-687.
- Shafer J. T., Brandon A. D., Lapen T. J., Righter M., Peslier A. H., and Beard B. L. 2010. Trace element systematics and  $^{147}Sm$ - $^{143}Nd$  and  $^{176}Lu$ - $^{176}Hf$  ages of Larkman Nuatak 06319: Closed-system fractional crystallization of an enriched shergottite magma. *Geochimica et Cosmochimica Acta* 74:7307-7328.
- Shearer C. K., Burger P. V., Papike J. J., Borg L. E., Irving A. J., and Herd C. 2008. Petrogenetic linkages among Martian basalts: Implications based on trace element chemistry of olivine. *Meteoritics & Planetary Science* 43:1241-1258.
- Shih C.-Y., Nyquist L. E., Wiesmann H., and Barrat J. A. 2003. Age and petrogenesis of picritic shergottite NWA 1068: Sm-Nd and Rb-Sr isotopic studies (abstract#1439). 36th Lunar and Planetary Science Conference. CD-ROM.

- Shih C.-Y., Nyquist L. E., Wiesmann H., Reese Y., and Misawa K. 2005. Rb-Sr and Sm-Nd dating of olivine-phyric shergottite Yamato 980459: Petrogenesis of depleted shergottites. *Antarctic Meteorite Research* 18:46-65.
- Shih C.-Y., Nyquist L. E., and Reese Y. 2007. Rb-Sr and Sm-Nd isotopic studies of Martian depleted shergottites SaU 094/005 (abstract#1745). 38th Lunar and Planetary Science Conference. CD-ROM.
- Shih C.-Y., Nyquist L. E., and Reese Y. 2009. Rb-Sr and Sm-Nd studies of olivine-phyric shergottites RBT 04262 and LAR 06319: Isotopic evidence for relationship to enriched basaltic shergottites (abstract#1360). 40th Lunar and Planetary Science Conference. CD-ROM.
- Shih C.-Y., Nyquist L. E., Reese Y., and Irving A. J. 2011. Rb-Sr and Sm-Nd ages, and petrogenesis of depleted shergottite Northwest Africa 5990 (abstract#1846). 42nd Lunar and Planetary Science Conference. CD-ROM.
- Smith J. V. and Steele I. M. 1984. Achondrite ALHA77005: Alteration of chromite and olivine. *Meteoritics* 19:121-133.
- Snyder G. A., Taylor L. A., and Neal C. R. 1992. A chemical model for generating the source of mare basalts: Combined equilibrium and fractional crystallization of the lunar magmasphere. *Geochimica et Cosmochimica Acta* 56:3809-3823.
- Stephen N. R., Genge M. J., Russell S. S., and Schofield P. F. 2013. Turning Tissint inside out; Searching for its launch pair(s) from Mars (abstract#2131). 44th Lunar and Planetary Science Conference. CD-ROM.
- Stolper E., McSween, Jr. H. Y., and Hays J. F. 1979. A petrogenetic model of the relationships among achondritic meteorites. *Geochimica et Cosmochimica Acta* 43:589-602.
- Symes S. J. K., Borg L. E., Shearer C. K., and Irving A. J. 2008. The age of the Martian meteorite Northwest Africa 1195 and the differentiation history of the shergottites. *Geochimica et Cosmochimica Acta* 72:1696-1710.
- Taylor L. A., Nazarov M. A., Shearer C. K., McSween, Jr. H. Y., Cahill J., Neal C. R., Ivanova M. A., Barsukova L. A., Lentz R. C., Clayton R. N., and Mayeda T. K. 2002. Martian meteorite Dhofar 019: A new shergottite. *Meteoritics & Planetary Science* 37:1107-1128.

- Treiman A. H., McKay G. A., Bogard D. D., Mittlefehldt D. W., Wang M.-S., Keller L., Lipshutz M. E., Lindstrom M. M., and Garrison D. 1994. Comparison of the LEW 88516 and ALHA77005 Martian meteorites: Similar but distinct. *Meteoritics* 29:581-592.
- Treiman A. H., Gleason J. D., and Bogard D. D. 2000. The SNC meteorites are from Mars. *Planetary and Space Science* 48:1213-1230.
- Udry A., Balta J. B., and McSween H. Y. 2013. CSD measurements on olivine grains in the Tissint meteorite (abstract#1266). 44th Lunar and Planetary Science Conference. CD-ROM.
- Usui T., McSween, Jr. H. Y., and Floss C. 2009. Petrogenesis of olivine-phyric shergottite Yamato 980459, revisited. *Geochimica et Cosmochimica Acta* 72:1711-1730.
- Vervoort J. D., Patchett P. J., Söderlund U., and Baker M. 2004. Isotopic composition of Yb and the determination of Lu concentrations and Lu/Hf ratios by isotope dilution using MC-ICPMS. *Geochemistry Geophysics Geosystems* 5:Q11002, doi:10.1029/2004GC000721.
- Warren P. H. and Wasson J. T. 1979. The origin of KREEP. *Reviews of Geophysics and Space Physics* 17:73-88.
- Warren P. H., Kallemeyn W. G., Arai T., and Kaneda K. 1996. Compositional-petrologic investigation of eucrites and the QUE94201 shergottite (abstract). *Antarctic Meteorites XXI*, pp.195-197.
- Wones D. R. and Gilbert M. C. 1969. The fayalite-magnetite-quartz assemblage between 600° and 800°C. *American Journal of Science* 267A:480-488.
- Wooden J. L., Shih C.-Y., Nyquist L. E., Bansal B. M., Wiesmann H., and McKay G, 1982. Rb-Sr and Sm-Nd isotopic constraints on the origin of EETA 79001: A second Antarctic shergottite. 13th Lunar and Planetary Science Conference, pp. 879-880.
- Zipfel J., Scherer P., Spettel B., Dreibus G. and Schultz L. 2000. Petrology and chemistry of the new shergottite Dar al Gani 476. *Meteoritics & Planetary Science* 35:95-106.

## Appendices

### Appendix 1. Rare earth element (REE) concentrations for pyroxene and plagioclase in Tissint.

Average and range of concentrations for pyroxene and plagioclase measured in this study. Concentrations reported are in ppm. Errors are 1 $\sigma$  standard deviation (SD).

#### Pyroxene (n = 5)

Element	Average	SD	Min	Max
La	0.126	0.099	0.029	0.251
Ce	0.441	0.352	0.100	0.891
Pr	0.089	0.073	0.013	0.198
Nd	0.636	0.506	0.161	1.233
Sm	0.451	0.325	0.092	0.847
Eu	0.199	0.098	0.082	0.317
Gd	0.949	0.673	0.204	1.780
Tb	0.204	0.139	0.053	0.382
Dy	1.392	1.002	0.328	2.810
Ho	0.303	0.203	0.078	0.578
Er	0.928	0.596	0.275	1.650
Tm	0.136	0.079	0.044	0.233
Yb	0.815	0.488	0.276	1.400
Lu	0.127	0.086	0.040	0.235
Hf	0.489	0.352	0.137	0.978

#### Plagioclase analyses (n = 2)

Element	Average	SD	Min	Max
La	0.029	0.709	0.024	0.034
Ce	0.109	2.203	0.093	0.125
Pr	0.024	0.434	0.014	0.034
Nd	0.234	3.264	0.234	0.234
Sm	0.152	2.034	0.119	0.184
Eu	0.705	0.595	0.472	0.938
Gd	0.488	3.601	0.488	0.488
Tb	0.100	0.688	0.100	0.100
Dy	0.720	4.589	0.720	0.720
Ho	0.173	1.002	0.173	0.173
Er	0.494	2.571	0.494	0.494
Tm	0.087	0.346	0.087	0.087
Yb	0.330	2.333	0.148	0.511
Lu	0.082	0.322	0.082	0.082
Hf	0.199	6.379	0.199	0.199

## Appendix 2. Compositions used for oxybarometry.

### Olivine-Pyroxene-Spinel oxybarometer

	17 / 9.	25 / 5.	4 / 1.	37 / 1.	38 / 1.
Oxide	Olivine	Pyroxene	Chromite 1	Chromite 2	Chromite 3
SiO <sub>2</sub>	36.20	54.90	0.109	0.229	0.280
TiO <sub>2</sub>	0.017	0.059	0.888	0.699	0.703
Al <sub>2</sub> O <sub>3</sub>	0.759	0.362	7.186	8.611	7.506
Fe <sub>2</sub> O <sub>3</sub>	0.000	0.000	2.161	1.648	2.928
Cr <sub>2</sub> O <sub>3</sub>	0.060	0.366	56.28	56.16	55.37
FeO	27.62	15.48	29.29	26.13	25.48
MnO	0.569	0.552	0.436	0.492	0.469
MgO	33.96	26.52	2.802	4.865	5.016
CaO	0.350	1.946	0.089	0.035	0.040
Na <sub>2</sub> O	0.000	0.011	0.000	0.010	0.000
Total	99.53	100.2	99.24	98.88	97.78
Fe#	31	25	86	76	76
Cr#	5	40	84	81	83

### Fe-Ti geothermometer

	40 / 1.	31 / 1.	33 / 1.	26 / 1.
Oxide	Ilmenite 1	Ilmenite 2	Ilmenite 3	Ilmenite 4
SiO <sub>2</sub>	0.134	0.190	0.195	0.083
TiO <sub>2</sub>	50.14	49.94	48.67	51.15
Al <sub>2</sub> O <sub>3</sub>	1.946	0.168	0.914	0.158
Fe <sub>2</sub> O <sub>3</sub>	2.426	3.927	4.300	3.084
V <sub>2</sub> O <sub>3</sub>	2.357	2.455	2.407	2.480
Cr <sub>2</sub> O <sub>3</sub>	0.677	0.406	0.227	0.162
FeO	40.02	41.35	41.17	43.32
MnO	0.727	0.728	0.720	0.719
MgO	2.478	1.579	1.021	1.003
CaO	0.083	0.191	0.256	0.208
Total	101.0	100.9	99.88	102.4

Fe-Ti geothermometer, continued. TM = titanomagnetite

Oxide	12 / 1. TM 1	21 / 3. TM 2	21 / 1. TM 3	16 / 3. TM 4	16 / 2. TM 5	16 / 1. TM 6	8 / 1. TM 7
SiO <sub>2</sub>	0.249	0.083	0.191	0.118	0.124	0.112	0.260
TiO <sub>2</sub>	23.34	23.68	23.49	22.99	24.84	24.30	25.30
Al <sub>2</sub> O <sub>3</sub>	2.890	3.212	3.396	2.940	2.821	2.884	1.859
Fe <sub>2</sub> O <sub>3</sub>	7.645	7.933	8.027	11.671	8.595	9.500	13.077
V <sub>2</sub> O <sub>3</sub>	1.555	1.418	1.382	1.362	1.444	1.459	1.437
Cr <sub>2</sub> O <sub>3</sub>	11.43	9.910	9.178	6.802	6.620	6.397	2.544
FeO	48.63	50.00	49.98	50.52	51.72	51.38	51.71
MnO	0.695	0.549	0.524	0.632	0.689	0.634	0.500
MgO	2.579	1.977	1.827	1.193	1.271	1.251	1.905
CaO	0.380	0.098	0.117	0.161	0.176	0.160	0.288
Total	99.38	98.86	98.11	98.39	98.30	98.07	98.88
Chr	16.95	14.72	13.79	10.30	9.989	9.697	3.861
Mt	10.68	11.26	11.48	16.79	12.36	13.68	18.10
Sp	6.389	7.114	7.605	6.637	6.346	6.516	4.206
Usp	65.87	66.94	67.13	66.24	71.32	70.08	73.05

### Appendix 3. Oxygen buffer equations.

The reactions and equations for oxygen buffers are listed below. These equations are based on a pressure of 1 bar and T (in Kelvins) is the calculated temperature from the oxybarometer.

Iron-Wüstite (IW)	$2\text{Fe}_x\text{O} = 2\text{Fe} + \text{O}_2$ Wustite Iron	(Frost, 1991)
$\log f_{\text{O}_2} = (-27578.7/T) + 6.790$	Herd (2008) using data from O'Neill and Pownceby (1993)	
Quartz-Fayalite-Magnetite (FMQ)	$2\text{Fe}_3\text{O}_4 + 3\text{SiO}_2 = 3\text{Fe}_2\text{SiO}_4 + \text{O}_2$ Magnetite Silica Fayalite	(Frost, 1991)
$\log f_{\text{O}_2} = (-25738/T) + 9.00$	Herd (2008) using data from Wones and Gilbert (1969)	
Magnetite-Hematite (MH)	$6\text{Fe}_2\text{O}_3 = 4\text{Fe}_3\text{O}_4 + \text{O}_2$ Hematite Magnetite	(Frost, 1991)
$\log f_{\text{O}_2} = (-25700.6/T) + 14.55$	Herd (2008) using data from Frost (1991)	